Fossil Bioapatites with Extremely High Concentrations of Rare Earth Elements and Yttrium from Deep-Sea Pelagic Sediments

Alain Manceau, Sophie Paul, Alexandre Simionovici, Valérie Magnin, Mélanie Balvay, Nathaniel Findling, Mauro Rovezzi, Samuel Muller, Dieter Garbe-Schönberg, Andrea Koschinsky

Geochemical and Mineralogical Characteristics of Extremely REY-rich Fossil Bioapatites from Deep-Sea Pelagic Sediments

Alain Manceau*[1], Sophie A.L. Paul[2,3], Alexandre Simionovici[1], Valérie Magnin[1], Mélanie Balvay[1], Nathaniel Findling[1], Mauro Rovezzi[4], Samuel Muller[5], Dieter Garbe-Schönberg[5,2], and Andrea Koschinsky[2]

[1]Univ. Grenoble Alpes, Univ. Savoie Mont Blanc, CNRS, IRD, ISTerre, 38000 Grenoble, France
[2]Department of Physics and Earth Sciences, Jacobs University Bremen, D-28759 Bremen, Germany
[3]GEOMAR, Helmholtz Centre for Ocean Research Kiel, Wischhofstr. 1-3, D-24148 Kiel, Germany
[4]Université Grenoble Alpes, CNRS, OSUG, FAME, F-38000 Grenoble, France
[5]CAU Kiel University, Institute of Geosciences, Ludewig-Meyn-Strasse 10, D-24118 Kiel, Germany

*Corresponding Author : alain.manceau@univ-grenoble-alpes.fr

ABSTRACT: Detailed geochemical and mineralogical insights into some of the richest rare earth elements and yttrium (REY)-containing bioapatites from ocean-floor sediments have been provided by combining laser ablation inductively coupled plasma mass spectrometry (LA-ICP-MS), electron probe microanalyses (EPMA), Rietveld X-ray diffraction analysis, and Ce L_3-edge high energy-resolution X-ray absorption near edge structure (HR-XANES) spectroscopy. Bioapatites at 1.94 and 4.70 meters below the seafloor (mbsf) of the Clarion-Clipperton Zone (CCZ) of the Pacific Ocean have 26,600 (RSD = 15.7%, *n* = 20) and 30,300 (RSD = 14.6%, *n* = 10) mg/kg (mg/kg) total REY, respectively, and bioapatites at 2.28 and 6.95 mbsf of the Peru Basin have 15,500 (RSD = 15.6%, *n* = 20) and 15,700 (RSD = 17.8%, *n* = 29) mg/kg total REY, respectively. All bioapatite specimens have a variety of isomorphic substitutions in all atomic positions of the crystallographic structure. The average crystallochemical formula of bioapatites at 6.95 mbsf of the Peru Basin is $[(PO_4)_{2.71}(SiO_4)_{0.04}(CO_3,SO_4)_{0.25}][Ca_{4.57}Na_{0.29}Y_{0.04}][F_{0.87}Cl_{0.21}]$. All other substituents are below 0.04 atoms per formula unit. HR-XANES provides the first direct evidence for trivalent Ce in sediment apatites. The strong negative geochemical anomaly of Ce in fossil bioapatites is well explained by

the occurrence of fourvalent Ce-MnO_2 and CeO_2 within the sediment and in seafloor ferromanganese nodules.

KEYWORDS: Cerium, apatite, REE, LA-ICP-MS, EPMA, HR-XANES

INTRODUCTION

How bioapatite (nominally $Ca_5(PO_4)_3(OH,F,Cl)$) from fossilized fish bones is enriched in rare earth elements and yttrium (REY) has been a primary focus of marine biogeochemistry,[1–11] since the discovery of REY-rich deep-sea muds in the Pacific Ocean.[12] The average REY concentrations of fossil bioapatites reported so far in pelagic sediments are 6107 mg/kg (RSD = 68.5%, *n* = 39) in the Central Indian Ocean Basin (CIOB),[3] 5779 mg/kg (RSD = 100%, *n* = 72) in the Tiki Basin in the Southeast Pacific (TKB),[3] 6361 mg/kg (RSD = 78.0, *n* = 184),[2] 14,126 mg/kg (RSD = 40.8%, *n* = 32)[4] and 6182 mg/kg (RSD = 71.8%, *n* = 79)[5] in the central North Pacific Ocean, and they range between 9300 and 32,000 mg/kg in the western North Pacific Ocean.[6] The enrichment in REY is considered to take place on the seafloor by post-mortem uptake during sedimentation and after burial through uptake from pore-waters during diagenesis.[5,7,13] Cerium (Ce) is enriched to a lesser extent than the other REY because of the oxidative scavenging of Ce(III) to Ce(IV) in contact with phyllomanganates of the birnessite group (δ-MnO_2)[14] present e.g. in ferromanganese nodules[15] and mineral coatings.[16] The relative depletion in Ce, referred to as the Ce anomaly, takes place under oxidizing conditions and is still observed over geological time long after the end of the enrichment process. Therefore, the Ce anomaly is used as a standard tool to assess paleo-redox conditions of ancient marine environments.

Cerium is usually considered to be trivalent in apatite substituted for Ca. Two coupled substitution schemes have been proposed to balance the excess of positive charge resulting from the heterovalent $Ce^{3+} \leftrightarrow Ca^{2+}$ substitution, $Ce^{3+} + Na^{+} \leftrightarrow 2Ca^{2+}$ and $Ce^{3+} + Si^{4+} \leftrightarrow Ca^{2+} + P^{5+}$.[17–21] Neither of them has been confirmed in sediment bioapatites. In addition, a study of fossil fish, shrimp, and crab tissues from the Late Cretaceous (95 Myr) showed that 20 ± 5% Ce was Ce(IV).[22] This result was obtained using Ce L_3-edge X-ray absorption near-edge structure (XANES) spectroscopy and, if it is confirmed on other bioapatites, will lead to rethink the use of the Ce anomaly as paleo-redox proxy as Ce(IV) is considered to be oxidized and sequestered only by MnO_2 in oxic environments.

Here, we use an integrated geochemistry and mineralogy approach to provide further insights into the enrichment of REY in marine sediment bioapatites More specifically, the aims of this study are (1) to report remarkably high REY concentrations in bioapatites from sediments sampled between 2 and 7 meters below the seafloor (mbsf) of the Clarion-Clipperton Zone (CCZ) and the Peru Basin of the Pacific Ocean, (2) to determine the oxidation state of cerium (Ce) in the bioapatites and the host sediments to help elucidate the chemical mechanism responsible for its geochemical anomaly and enrichment in apatite, and (3) to calculate the crystallochemical formula of the bioapatites to inform the charge compensation mechanism of the $REY^{3+} \leftrightarrow Ca^{2+}$ substitution. The mineralogy and chemical composition of the sediments were obtained using bulk Rietveld X-ray diffraction and inductively coupled plasma mass spectrometry (ICP-MS), and the chemical composition of the bioapatites were obtained using electron probe microanalyses (EPMA) and laser ablation ICP-MS (LA-ICP-MS). The oxidation state of Ce in the sediments and bioapatites was obtained using Ce L_3-edge high energy-resolution X-ray absorption near edge structure (HR-XANES) spectroscopy (also designated HERFD XANES[23]). HR-XANES spectroscopy has better sensitivity to Ce oxidation state and speciation than standard XANES spectroscopy.[24,25]

MATERIALS AND METHODS

Samples. Core 16GC was collected in 2019 in the CCZ during RV SONNE cruise SO268, and core 51GC was collected in 2015 in the Peru Basin during RV SONNE cruise SO242/1, both using a gravity corer (GC) (Figure S1 and Table S1).[26–28] Upon core retrieval, GCs were cut into one meter sections that were split into a working and an archive half. The working half was immediately transferred into the cold room of RV SONNE (ca. 4°C) for sampling under close to in situ temperature conditions. Sampling was conducted immediately to minimize contact with ambient air and acid clean materials were used. Two samples were recovered from each core for this study, at 1.94 (16GC-194) and 4.70 (16GC-470) mbsf for 16GC, and at 2.28 (51GC-228) and 6.95 (51GC-695) mbsf for 51GC. Oxygen penetration depths in the CCZ are several meters, and therefore 16GC was completely oxic.[26,29] In contrast, 51GC is suboxic, because the Peru Basin seafloor receives more organic matter than the CCZ and oxygen penetration depths are only ca. 15 cm.[30,31]

Based on extrapolation of sedimentation rates of the surface sediment in the eastern CCZ[32] (0.35-0.6 cm/ka) and the Peru Basin[30] (0.4 cm/ka), we estimate an age of roughly 332-554 ka for layer 1.94 m and 783 ka -1.34 Ma for layer 4.70 m of 16GC, and 570 ka for layer 2.28 m and 1.74 Ma for layer 6.95 m of 51GC. It needs to be taken into account, however, that the sedimentation

rate has likely changed over time, the deeper the layer the larger is the impact of compaction and that part of the GC surface is often lost during sampling (ca. 75 cm and 15 cm for 16GC and 51GC, respectively) which we cannot account for in this basic age estimation.

X-ray diffraction. The XRD patterns of the four sediments and apatite grains of 51GC-228 were measured using a D8 Advance de Bruker Axs diffractometer and CuKα radiation at 40 kV and 40 mA over a 2θ range of 5-90°. Mineral phases were identified with the ICDD powder diffraction database, and their amounts quantified using the Rietveld BGMN program[33] implemented with the Profex graphical user interface.[34] With the exclusion of apatite, minor phases with concentrations ≤ 1 weighted % were excluded from the refinement iterations in order to constrain the final results.

ICP-MS. Geochemical analyses of the bulk sediment were conducted at Jacobs University Bremen. Sediment from which pore water had been previously extracted by centrifugation were dried and homogenized. 50-100 mg were then acid pressure digested using a PicoTrace DAS system with suprapure $HClO_4$ and HF at 220°C for 12 h. After evaporation and two times addition of HCl and re-evaporation, samples were taken up in 0.5 M HNO_3 and 0.5% HCl (v/v). REY were analyzed with quadrupole ICP-MS (Perkin Elmer Nexion 350x). The certified reference materials BHVO-2, MESS-3 and MESS-4 were used to check accuracy and measured values generally fit well with available certified values. Data were corrected for interferences of Ba on Eu, and LREE oxides and hydroxides on HREE, by experimentally determined matrix-matched oxide and hydroxide yields of molecular ions based on Dulski (1994).[35]

LA-ICP-MS. The LA-ICP-MS analyses were performed on epoxy mounted polished sections, either of individual apatite grains hand-picked under a binocular (16GC-194, 16GC-470, 51GC-228), or of the whole sediment (51GC-695) (Figure S2). The number of mineral grains and total number of measured spots of 16-44 µm in size are (10, 20) for 16GC-194, (10, 10) for 16GC-470, (10, 20) for 51GC-228, and (12, 29) for 51GC-695. In addition, nine measurements were performed in the clayey matrix of 51GC-695 away from apatite grains with a spot size of 90 µm. Measurements were conducted on-mass in no-gas mode using an AGILENT 8900 ICP-MS/MS instrument coupled to a COHERENT 193 nm GeoLas HD laser ablation unit. The laser was operated with 10 Hz pulse frequency at a fluence of 3 J cm^{-2}. Calibration and control of reproducibility over the course of the analyses were carried out with an international reference material carbonatite USGS-COQ-1NP prepared as a nano-particulate pressed powder tablet and a protocol described previously.[36,37] Durango apatite from Gerin et al. (2017)[38] and synthetic hydroxyapatite USGS-MAPS-4 were analyzed together with the samples. The REY concentrations

between individual measurements were uniform with an uncertainty of 1SD, <4% RSD. The 12 grains of 51GC-695 were analyzed by EPMA prior to the LA-ICP-MS measurement. REY concentrations were normalized to the Post-Archean Australian Shale (PAAS) concentrations reported by McLennan.[39,40]

EPMA. Quantitative chemical analyses of apatite crystals for 51GC-695 were performed at ISTerre using a JEOL JXA-8230 electron microprobe equipped with five wavelength-dispersive spectrometers (WDS) and an energy-dispersive detector. The polished section of the epoxy embedded whole sediment was coated with a few tens of nm graphite film and analyzed for major and trace elements using an acceleration voltage of 15 kV, a beam current of 20 nA, and a spot size of 5 μm. Volatile F and Cl were analyzed first and with shorter counting times (10-20 s) in order to suppress possible diffusion.[41] Two apatites from Durango, Mexico, were measured, the one previously analyzed by Gerin et al.[38] and a reference from P&H Developments Ltd. that served as quality control (QC) material. Details on analytical precisions and determination of detection limits can be found in Batanova et al.[42]

HR-XANES. The Ce L_3-edge HR-XANES spectra of single apatite grains and pressed pellets of the bulk sediments were measured at the French CRG FAME-UHD (BM16) beamline of the European Synchrotron Radiation Facility (ESRF) together with the following references: the Durango apatite from Gerin et al. (2017)[38] (Ce(III)), $Ce(NO_3)_3 \cdot 6H_2O$ (Ce(III)), cerianite ($Ce(IV)O_2$), and an hydrogenic nodule from the Indian Ocean (D20-1B[43]) (Ce(IV)-sorbed MnO_2). The Ce $L_{\alpha 1}$ ($3d_{5/2} \rightarrow 2p_{3/2}$) fluorescence line was selected using the 331 reflection of five Ge crystals of 100 mm diameter, spherically bent to a radius of 1.0 m.[44,45] The Bragg angle of the spectrometer was 84.7° in a vertical Rowland circle geometry. The diffracted intensity was measured with a Si drift diode detector (SDD) in single photon counting mode. The effective energy resolution calculated from the full width at half maximum (FWHM) of the $Ce(NO_3)_3 \cdot 6H_2O$ white-line was about 3.2 eV, compared to 6.1 eV when using an energy-dispersive detector. The incoming photon energy was selected by a cryogenically cooled double Si(220) monochromator and calibrated by assigning the maximum of the derivative of the K-edge spectrum for elemental V to be 5465.0 eV. The stability in energy (better than 0.1 eV) was monitored with the V foil placed behind the sample pellets. The HR-XANES spectra were measured from 5690 eV to 5850 eV and normalized to unity at E = 5850 eV. All measurements were performed at a temperature of 10-15 K using a helium flow cryostat. No changes in spectral features were noted during the course of data collection that would indicate radiation damage.

RESULTS

Mineralogy of the bulk sediments. Circa 50% of the sediments consists of clay dominated by Ca-smectite with minor muscovite and trace of chlorite (Table S2). The other phases systematically present in subordinate amounts (< 10%) are quartz, plagioclase, phillipsite, halite, and barite (Figure S3). Gypsum occurs in 51GC-228 and 51GC-695 (1-2%), and calcite, in the form of coccolith, occurs in 51GC-228 (6.8%) (Figure S4). The XRD pattern of the apatite grains shows broad maxima from poorly-crystallized apatite along with calcite and quartz diffraction peaks from impurities (Figure S5).

REY composition of the bulk sediments and bioapatites. The REY and REE contents of the bulk sediments are 326 and 256 mg/kg for 16GC-194, 470 and 363 mg/kg for 16GC-470, 256 and 181 mg/kg for 51GC-228,[46] and 592 and 376 mg/kg for 51GC-695[46] (Tables 1 and S3). These concentrations are on the low end-side of REY-rich deep-sea muds.[1–8,47] The REY contents of the 16GC core are, however, typical of the CCZ concentrations.[7] The fossil bioapatites contain on average 78.1 (16GC-194, n = 20) and 64.6 (16GC-470, n = 10), 60.5 (51GC-228, n = 20) and 26.6 (51GC-695, n = 29) times more REY than the bulk sediments (Table 1). A comparison with previous studies on bioapatites shows that the CCZ apatites contain the highest amounts of total REY reported to date and the Peru Basin apatites are only equaled by the REY-rich deep-sea mud from Minami-Torishima Area (MTA), Southeastern Japan (Figure 1).[3,2,4,5]

Plotting together the four shale-normalized REY patterns for the bulk sediments shows the following traits (Figure 2a). The two sediment cores differ in their enrichment profiles. The 16GC core is most enriched in middle REE (MREE), and the 51GC core is most enriched in heavy REE (HREE). The four patterns display a more or less prominent negative Ce anomaly, and the 51GC REY pattern has a positive Y anomaly. When superimposed, the REY patterns of the sediment matrix (n = 9) and apatites (n = 29) for 51GC-695 are similar (Figure 2b), despite the apatites being on average 35.7 times richer in REY than the matrix (Table 1). The quantitative uptake of REY in apatites from sediment pore solutions is therefore achieved without fractionation. The light REE (LREE) pattern of apatites in 51GC shows considerable similarity with the MTA pattern, but the 51GC apatites are more enriched in HREE than the MTA apatites (Figure 2c). It was seen previously that the 16GC apatites contained a record amount of total REY. Figure 2c shows that these apatites are also richest on average in all individual REY elements when compared to the fossil bioapatites analyzed previously.[3,2,4,5]

The Ce anomaly $(Ce/Ce^*)_{SN}$ was calculated as the shale-normalized (SN) average concentration of Ce relative to those of La and Pr. It is positive when $(Ce/Ce^*)_{SN} > 1$, and negative when $(Ce/Ce^*)_{SN} < 1$. Two equations are commonly used, $A1 = Ce/(La \times Pr)^{0.5}$,[15] and $A2 = Ce/(0.5 \times La + 0.5 \times Pr)$.[48] If the Ce, La, and Pr concentrations are from independent measurements, the uncertainty on the average Ce anomaly can be expressed in terms of the 1SD (noted σ) of the Ce, La, and Pr concentrations using the following propagation equation[49]

$$\sigma_A^2 = \sigma_{Ce}^2\left(\frac{\partial A}{\partial Ce}\right)^2 + \sigma_{La}^2\left(\frac{\partial A}{\partial La}\right)^2 + \sigma_{Pr}^2\left(\frac{\partial A}{\partial Pr}\right)^2.$$

Carrying out the math for the uncertainties of the A1 and A2 equations yields:

$$\sigma_{A1} = A1\sqrt{\left(\frac{\sigma_{Ce}}{Ce}\right)^2 + \left(\frac{\sigma_{La}}{La+Pr}\right)^2 + \left(\frac{\sigma_{Pr}}{La+Pr}\right)^2}$$

$$\sigma_{A2} = A2\sqrt{\left(\frac{\sigma_{Ce}}{Ce}\right)^2 + \frac{\sigma_{La}^2 + \sigma_{Pr}^2}{[2(La+Pr)]^2}}$$

Equations A1 and A2 give the same result to the nearest one-hundredth (Table 1). Because 51GC samples have a positive La anomaly, the abovementioned equations slightly overestimate the negative Ce anomaly. In such case, an alternative is to calculate the Ce anomaly using the Pr and Nd concentrations[50] or the Ce/Pr ratios[51]. As this would not change the overall interpretation of the data, we use the more commonly applied equations for comparability.

The two 16GC bulk sediments have a weak negative Ce anomaly (0.63 and 0.55) and their apatites have a stronger Ce anomaly (0.29(8) and 0.22(5)). The two 51GC bulk sediments have in contrast a moderately negative Ce anomaly (0.53 and 0.31), but their apatites also have a stronger Ce anomaly (0.37(9) and 0.22(7)). The Ce anomaly of the 51GC-695 matrix is 0.33(12), that is 0.02 less negative than that of the bulk sediment (0.31), because the latter includes apatites that are more depleted in Ce (A1 = 0.22(7)) than the Ce-host phases present in the clayey matrix.

Chemical composition of apatites. Forty-one point EPMA were performed on the 51GC-695 apatite grains (n = 12) analyzed subsequently by LA-ICP-MS (Table S4). In general, they confirm the compositional variability observed by LA-ICP-MS between apatites and between individual points of measurements on a same grain. In addition to REY, the fossil bioapatites are enriched in Na (1.22 ± 0.24 wt %), F (2.97 ± 0.49 wt %), and Cl (1.33 ± 0.40 wt %), and to a lesser extent in Si (0.20 ± 0.21 wt %) and Sr (0.11 ± 0.06 wt %). Thus, they have a variety of isomorphic substitutions in all structural positions of the stoichiometric $Ca_5(PO_4)_3(OH,F,Cl)$ apatite formula, which is a

typical feature for most natural specimens.[18,52,53] The REY contents of the coccoliths for 51GC-228 were all below the detection limit of EPMA (Table S5).

Oxidation state of Ce. Following the dipole selection rules, electrons are excited at the Ce L_3-edge from the $2p_{3/2}$ core level into unoccupied $5d_{5/2}$ states. The $2p_{3/2} \rightarrow 5d_{5/2}$ transition gives rise to a single peak for Ce(III) and a doublet for Ce(IV), a difference widely used to distinguish the two oxidation states in earth materials (Figure 3a).[11,15,22,54–62] The higher chemical resolution obtained here by measuring the XANES spectra with a spectrometer[44] (i.e., HR-XANES mode) is illustrated in Figures 3a,b. The resulting spectral sharpening is noteworthy, and clearly aids in a better discrimination of Ce(III) and Ce(IV), on one hand, and of Ce(IV)-MnO_2 and CeO_2, on the other hand.

Three apatite grains were measured for each sediment and were found to be statistically identical (Figure S6). Therefore, the 12 spectra were averaged to obtain one spectrum representative of the sediment bioapatites. This spectrum is similar to those of the Durango apatite and $Ce(III)(NO_3)_3 \cdot 6H_2O$ (Figure 3a,c). The 51GC-228 bulk sediment also contains only Ce(III), with a limit of detection for Ce(IV) estimated to 8 atom % (Figure 3d). In contrast, 51GC-695 and the two 16GC bulk sediments contain some Ce(IV) seen as a shoulder at 5732 eV and an increase of the intensity at 5740 eV on their HR-XANES spectra (Figure 3d). The 5740 eV absorption feature is present on the $Ce(III)(NO_3)_3 \cdot 6H_2O$ spectrum measured at high resolution (Figure 3a), and therefore this structure is not diagnostic for Ce(IV), as suggested previously from the lower resolution XANES measurement of fossil fish, shrimp, and crab tissues from the Late Cretaceous.[22] A linear fit of the 51GC-228 bulk sediment spectrum and the Ce(IV)-MnO_2 reference to the 51GC-695 and 16GC data yielded 24% Ce(IV) for 51GC-695, 31% Ce(IV) for 16GC-194, and 38% for 16GC-470 with a precision of 4% to total Ce (Figure S7a,b,c). Replacing Ce(IV)-MnO_2 with CeO_2 in the fit did not improve the fit quality (Table S6). In contrast, inclusion of CeO_2 in the fit clearly provided a better description of the data for 16GC-470 with approximately 47% Ce(IV) (Figure S7d, Table S6). The lesser amount of Ce(IV) in 51GC (0 - 24%) than in 16GC (31 - 47%) is consistent with the suboxic conditions of the 51GC sediment and the resulting dissolution of MnO_2.

DISCUSSION

This study provides detailed insights into the mineralogy of the CCZ and Peru Basin muds, the geochemical enrichment of Ce and other REY elements in fossil bioapatite, its chemical composition, and the oxidation state of Ce in apatite and the sediment host matrix. Thanks to its

enhanced sensitivity and resolution, Ce L_3-edge HR-XANES appears to be the most straightforward and reliable way to assess the oxidation state of Ce and the identity of the Ce phase in earth materials. Besides Ce, this technique has been used previously for the distinction of the As(-I)/As(III)/As(V),[63,64] Se(-I)/Se(IV)/Se(VI),[63] Eu(II)/Eu(III),[65] Au(0)/Au(I)/Au(III),[66–72] Tl(I)/Tl(III)[43], U(IV)/U(V)/U(VI),[73,74] and Hg(0)/Hg(II)[75,76] oxidation states.

Amount of apatite. Quantification of the apatite contents was not possible by XRD, because their amounts fell below the limit of detection (LoD). Specific detection limits in Rietveld analysis are difficult to establish for they depend on many factors, including the quality of the recorded data, the exact type of the crystalline phase, its crystallinity, its chemical composition, and the chemical and mineral composition of the batch sample. A conservative LoD value is 1 wt %.[77,78] This estimate can be benchmarked by the elemental analyses of 51GC-695 for which we have the REY compositions of the bulk, the clayey matrix (n = 9), and the apatite grains (n = 29). Carrying the calculation yields 1.2 ± 0.2 wt % apatite to total mineral phases (Table 1).

Geochemical enrichment in REY. Despite being an accessory mineral in the studied muds, the REY are strongly partitioned in apatite. The approximately 30 to 70 times enrichment in REY of fossil bioapatites relative to the clayey matrix, compounded by their trace amounts, yields extremely high REY concentrations. However, with only 1 wt % apatite in bulk sediment, the clayey matrix contains the greatest proportion of the whole-sediment abundance of REY,[79] despite the much lower weight concentration of REY in bulk sediment. The contribution of the apatite reservoir to the total Ce content is also small in phosphatized marine ferromanganese nodules.[62] This finding from the direct physical measurement presented here contrasts with the findings from recent sequential extraction where approx. > 70% of REY – except Ce – were found in the phosphate leachate.[3,7] Although valuable in their own right, sequential extractions are naturally limited because of the indirect nature of the identified specific phases.[80,81] The selectivity of the bioapatite leaching step used in previous studies[3,7] of chemically and physically complex sediments is unknown.

All REY apparently have the same affinity for apatite, as suggested by the similarity of the REY patterns of the clayey matrix and apatites in 51GC-695 (Figure 2b). This is also reflected in the small standard deviation (4.2) of the 35.5 times enrichment in REY of the 51GC-695 apatites relative to the clayey matrix (Table 1). The enrichment factor of Ce in the 51GC-695 apatites is only 22.9, therefore notably outside the distribution range of the other REY values. This finding suggests that Ce is strongly bound to another mineral phase. One possibility is a birnessite-like

phase (δ-MnO_2),[14] as Ce(III) is oxidatively scavenged to Ce(IV) by phyllomanganates of this family[15] and the Ce(IV)-MnO_2 association common in marine ferromagnaese deposits.[15,82] Occurrence of Ce(IV)-MnO_2 is supported by the detection of 24 ± 4% Ce(IV) in bulk 51GC-695 using HR-XANES. Minor cerianite (CeO_2) as an admixture to Ce(IV)-MnO_2 cannot be excluded, however, because this mineral is detected in 16GC-470 which has 38 ± 4% Ce(IV) (Figure S7d, Table S6). The co-occurrence of Ce(IV)-MnO_2 and CeO_2 has been reported previously by Marcus et al.[62] in a deep-sea ferromanganese nodule from the South Pacific.

The oxidative scavenging of Ce(III) to less soluble Ce(IV) on particles in the water column and at the surface of Mn oxides on the seafloor and seamounts yields a positive geochemical anomaly ($(Ce/Ce^*)_{SN} > 1$) in FeMn crusts and nodules and a resulting negative anomaly ($(Ce/Ce^*)_{SN} < 1$) in seawater and the Ce(III) host minerals.[15] Therefore, the lower negative Ce anomalies (i.e., closer to 1) of the 16GC-194, 16GC-470, and 51GC-695 bulk sediments compared to the constituent apatites is well explained by the occurrence of Ce(IV) detected by HR-XANES in the three sediments. Indeed, the Ce anomaly measured in the bulk is a weighted-average of the positive Ce(IV)-MnO_2 and CeO_2 anomalies and the negative anomaly of Ce(III) present in apatite and clay minerals. When the Ce(III)-apatite contribution is eliminated by measuring the REY concentrations directly in the clayed matrix away from the apatite grains (51GC-695), the Ce anomaly increases by 0.33 – 0.31 = 0.02 relative to the bulk measurement, as expected (Table 1).

Occurrence of Ce(IV) forms in sediments is consistent with the depletion in Ce of pore-waters measured at 5-6 mbsf.[7] However, there is no correlation between the bulk Ce anomalies and the %Ce(IV) in the sediments (Figure S8a), nor between the difference of Ce anomaly in the bulks and the constituent apatites, on one hand, and the %Ce(IV) in the sediments, on the other hand (Figure S8b). The lack of correlation indicates that the Ce geochemistry did not reach thermodynamic equilibrium at several meters below the seafloor, which is also supported by the coexistence of several Ce(IV) and Ce(III) forms. We conclude from this that the Ce anomaly of apatites is at least partly inherited from the time of their enrichment in REY at the surface of the seafloor or immediately beneath during early diagenesis, as suggested previously.[2]

Chemical formula of apatites. A caveat in the EPMA is the total weight percents of 88.0 ± 1.4%, which are much lower than 100 wt % when all elements are analyzed and the quantification accurate (Table S4). Previous EPMA of fossil bioapatites by Liao et al. (2019, 2022)[3,5] and Bi et al. (2021)[2] also deviate from 100 wt %, summing up to 86.9 ± 8.6% (n = 58),[5] 82.9 ± 9.6% (n = 184),[2] and 84.0 ± 5.5% (n = 111).[3] Here, experimental errors due to calibration of the X-ray fluorescence

intensity with mineral standards and to the measurement protocol, such as background subtraction, can be dismissed because the Durango reference has a weight percent total of 99.5 ± 0.3% (n = 8) (Table S4). One reason for the difference to 100% is the intensity loss resulting from the high porosity and surface roughness of bioapatite, which prevent the preparation of flat micropolished sections conventionally used for quantification procedures in EPMA.[83–85] Another reason is the occurrence in the structure of unmeasured light elements, such as C and H, in the form of carbonate, hydroxyl groups possibly replaced by water molecules,[86] and perhaps organic matter. Carbonate groups can replace phosphate groups in sediment apatites according to the coupled CO_3^{2-} + F^- substitution for PO_4^{3-},[87,88] as in the carbonate fluorapatite francolite.[89] Carbonate substitution was verified by infrared spectroscopy. Bioapatites display a broad peak at 1430 cm^{-1} assigned to the ν_3 CO_3 band (Figure S9a).[90–93] This peak is absent in the Durango apatite which is magmatic-hydrothermal[94] (Figure S9b). Sulfur, which was not measured, typically amounts to less than 2.0 wt % in bioapatite from deep-sea pelagic sediments.[3,2,4,5] Notwithstanding the exact reasons for the deviation of the chemical sums from 100 wt % total, a plot of the concentrations of the four REY detected by EPMA (Y, La, Ce, Nd) and their concentrations measured by LA-ICP-MS shows excellent agreement between the two analyses (Table S7 and Figure S10, R^2 = 0.996).

The chemical formulae of the 41 spots measured by EPMA on the 12 apatites of 51GC-695 were calculated first on the basis of 8 cations per formula unit (pfu) (Table S4). The average numbers of major elements are 4.72(8) Ca, 2.80(6) P, 0.30(6) Na, 0.90(15) F, and 0.22(6) Cl pfu (n = 41), compared to the theoretical stoichiometry of $Ca_5(PO_4)_3F$ for fluorapatite and the measured formula of $(Ca_{4.95}Na_{0.04}La_{0.02}Ce_{0.02})((P_{2.96}Si_{0.03})O_4)_{3.00}F_{0.95}Cl_{0.06}$[95] for the Durango reference (Table S4). The Si and Y contents are 0.04(4) and 0.04(1) pfu, respectively, Al, Fe, Mn, Sr, La, and Nd are between 0.01 and 0.03 pfu, and all other substituents are below 0.01 pfu. The compositional variability among the apatites is larger than the analytical uncertainties, which are of the order of 0.01 to 0.02 pfu (Table S4). The analyzed apatites contain under the 8 cations total scheme 2.84(6) P + Si pfu, 5.16(6) Ca + Na + Y pfu in the two Ca sites, and 1.11(13) F + Cl pfu. The 0.16 excess of cations in the Ca sites is at least partly due to the lack of C and S in the analysis and the assumption of 8 cations pfu in the calculation of the chemical formulae. Recalculating the number of atoms pfu with the assumption of 5 cations in the Ca sites yields: 2.71(9) P, 0.04(4) Si, 4.57(6) Ca, 0.29(6) Na, 0.04(4) Y, 0.87(14) F, and 0.21(6) Cl pfu, with all other elements below 0.04 pfu. The total number of P and Si atoms in the P site is now 2.75(10) pfu, suggesting that this site may contain approximately 0.25 pfu CO_3^{2-} and SO_4^{2-} ions. Incorporation of CO_3^{2-} ions in the P site, commonly

observed in sedimentary fluorapatites[52,96] in contrast to magmatic-hydrothermal apatites, is further suggested by (1) the (0.87 + 0.21) – 1.0 = 0.08 pfu excess of F + Cl in the structure with formation of CO_3F^{3-} species,[87] and (2) the high amount of Na to balance the electronic charge deficit caused by the CO_3^{2-} for PO_4^{3-} substitutions with parallel Na^+ for Ca^{2+} substitutions.[52] Atomistic calculation of the incorporation of Nd in fluorapatite predicts that the $Nd^{3+} \leftrightarrow Ca^{2+}$ substitution is charge compensated by parallel $Si^{4+} \leftrightarrow P^{5+}$ substitution preferably to $Na^+ \leftrightarrow Ca^{2+}$ substitution.[97] The identical pfu value of 0.04(4) for Si and Y provides suggestive evidence for coupled Si-REY substitution in bioapatite. Under these schemes, and omitting the possible presence of vacancies[86], OH groups, and water molecules in the channels of the apatite framework, a general crystallochemical formula is $[(PO_4)_{2.71}(SiO_4)_{0.04}(CO_3,SO_4)_{0.25}][Ca_{4.57}Na_{0.29}Y_{0.04}][F_{0.87}Cl_{0.21}]$. This formula is probably generic to seafloor sediment apatites,[2–6,86] as all substituents have been identified previously in fossil bioapatites.

In this work, we have shown that Ce is incorporated in trivalent form in fossil bioapatites from two sediment cores of the Pacific Ocean. Enrichment in REY is considered to occur by a diffusion mechanism into the apatite nanopores, rather than by precipitation of authigenic apatite. Future research will be devoted to testing this hypothesis directly from the structural incorporation of REY into the apatite structure.

ASSOCIATED CONTENT

Supporting Information

The Supporting Information is available free of charge on the ACS Publications website at DOI:

Geographical location of the 16GC and 51GC cores, optical and electronic images of bioapatites, XRD patterns, Ce L_3-edge HR-XANES spectra of bioapatites with fits, infrared spectra, relationship between the Ce anomaly and the percentage of Ce(IV), and plot of the Y, La, Ce, and Nd concentrations measured by LA-ICP-MS and EPMA (PDF)

Sediment core information, XRD Rietveld refinement, LA-ICP-MS and EPMA analyses, results of HR-XANES fits, and Y, La, Ce, and Nd concentrations measured by LA-ICP-MS and EPMA (XLSX)

AUTHOR INFORMATION

Corresponding Authors

E-mail: alain.manceau@univ-grenoble-alpes.fr

Notes

The authors declare no competing financial interests.

ACKNOWLEDGEMENTS. James Hein provided the D20-1B sample and Cécile Gautheron provided the Durango apatite. We thank Inken Preuss, Tim Jesper Suhrhoff, Annika Moje and Erika Kurahashi for help with sampling at sea and analyses at Jacobs University Bremen. Angela Trumpf and Jonas Lobbel, CAU Kiel, helped with the preparation of nanoparticulate powder tablets. Infrared spectra were collected at the Institut de Planétologie et d'Astrophysique (IPAG) in Grenoble with the support of Pierre Beck. Support was provided to A.S. by the Institut Universitaire de France (IUF). ISTerre is part of Labex OSUG@2020 (ANR10 LABX56). Part of this work was funded by the German Federal Ministry of Education and Research (BMBF) in the framework of the JPI Oceans project MiningImpact (grant nos. 03F0707G and 03F0812G to Andrea Koschinsky). The SOLEIL facility provided synchrotron beamtime via the French CRG program at ESRF (proposal #20210014).

REFERENCES

(1) Kato, Y.; Fujinaga, K.; Nakamura, K.; Takaya, Y.; Kitamura, K.; Ohta, J.; Toda, R.; Nakashima, T.; Iwamori, H. Deep-Sea Mud in the Pacific Ocean as a Potential Resource for Rare-Earth Elements. *Nature Geosci.* **2011**, *4*, 535–539.

(2) Bi, D.; Shi, X.; Huang, M.; Yu, M.; Zhou, T.; Zhang, Y.; Zhu, A.; Shi, M.; Fang, X. Geochemical and Mineralogical Characteristics of Deep-Sea Sediments from the Western North Pacific Ocean: Constraints on the Enrichment Processes of Rare Earth Elements. *Ore Geol. Rev.* **2021**, *138*, n° 104318.

(3) Liao, J.; Chen, J.; Sun, X.; Wu, Z.; Deng, Y.; Shi, X.; Wang, Y.; Chen, Y.; Koschinsky, A. Quantifying the Controlling Mineral Phases of Rare-Earth Elements in Deep-Sea Pelagic Sediments. *Chem. Geol.* **2022**, *595*, n° 120792.

(4) Takaya, Y.; Yasukawa, K.; Kawasaki, T.; Fujinaga, K.; Ohta, J.; Usui, Y.; Nakamura, K.; Kimura, J. I.; Chang, Q.; Hamada, M.; Dodbiba, G.; Nozaki, T.; Iijima, K.; Morisawa, T.; Kuwahara, T.; Ishida, Y.; Ichimura, T.; Kitazume, M.; Fujita, T.; Kato, Y. The Tremendous Potential of Deep-Sea Mud as a Source of Rare-Earth Elements. *Sci. Rep.* **2018**, n° 5763.

(5) Liao, J.; Sun, X.; Li, D.; Sa, R.; Lu, Y.; Lin, Z.; Xu, L.; Zhan, R.; Pan, Y.; Xu, H. New Insights into Nanostructure and Geochemistry of Bioapatite in REE-Rich Deep-Sea Sediments: LA-ICP-MS, TEM, and Z-Contrast Imaging Studies. *Chem. Geol.* **2019**, *512*, 58–68.

(6) Kon, Y.; Hoshino, M.; Sanematsu, K.; Morita, S.; Tsunematsu, M.; Okamoto, N.; Yano, N.; Tanaka, M.; Takagi, T. Geochemical Characteristics of Apatite in Heavy REE-Rich Deep-Sea Mud from Minami-Torishima Area, Southeastern Japan. *Res. Geol.* **2014**, *64*, 47–57.

(7) Paul, S. A. L.; Volz, J. B.; Bau, M.; Koster, M.; Kasten, S.; Koschinsky, A. Calcium Phosphate Control of REY Patterns of Siliceous-Ooze-Rich Deep-Sea Sediments from the Central Equatorial Pacific. *Geochim. Cosmochim. Acta.* **2019**, *251*, 56–72.

(8) Yasukawa, K.; Nakamura, K.; Fujinaga, K.; Machida, S.; Ohta, J.; Takaya, Y.; Kato, Y. Rare-Earth, Major, and Trace Element Geochemistry of Deep-Sea Sediments in the Indian Ocean: Implications for the Potential Distribution of REY-Rich Mud in the Indian Ocean. *Geochem. J.* **2015**, *49*, 621–635.

(9) Yasukawa, K.; Liu, H.; Fujinaga, K.; Machida, S.; Haraguchi, S.; Ishii, T.; Nakamura, K.; Kato, Y. Geochemistry and Mineralogy of REY-Rich Mud in the Eastern Indian Ocean. *J. Asian Earth Sci.* **2014**, *93*, 25–36.

(10) Kashiwabara, T.; Toda, R.; Fujinaga, K.; Honma, T.; Takahashi, Y.; Kato, Y. Determination of Host Phase of Lanthanum in Deep-Sea REY-Rich Mud by XAFS and μ-XRF Using High-Energy Synchrotron Radiation. *Chem. Lett.* **2014**, *43*, 199–200.

(11) Kashiwabara, T.; Toda, R.; Nakamura, K.; Yasukawa, K.; Fujinaga, K.; Kubo, S.; Nozaki, T.; Takahashi, Y.; Suzuki, K.; Kato, Y. Synchrotron X-Ray Spectroscopic Perspective on the Formation Mechanism of REY-Rich Muds in the Pacific Ocean. *Geochim. Cosmochim. Acta.* **2018**, *240*, 274–292.

(12) Toyoda, K.; Tokonami, M. Diffusion of Rare-Earth Elements in Fish Teeth from Deep-Sea Sediments. *Nature* **1990**, *345*, 607–608.

(13) Reynard, B.; Lecuyer, C.; Grandjean, P. Crystal-Chemical Controls on Rare-Earth Element Concentrations in Fossil Biogenic Apatites and Implications for Paleoenvironmental Reconstructions. *Chem. Geol.* **1999**, *155*, 233–241.

(14) Manceau, A.; Marcus, M. A.; Grangeon, S.; Lanson, M.; Lanson, B.; Gaillot, A. C.; Skanthakumar, S.; Soderholm, L. Short-Range and Long-Range Order of Phyllomanganate

Nanoparticles Determined Using High Energy X-Ray Scattering. *J. Appl. Crystallogr.* **2013**, *46*, 193–209.

(15) Takahashi, Y.; Manceau, A.; Geoffroy, N.; Marcus, M. A.; Usui, A. Chemical and Structural Control of the Partitioning of Co, Ce, and Pb in Marine Ferromanganese Oxides. *Geochim. Cosmichim. Acta* **2007**, *71*, 984–1008.

(16) Manceau, A.; Lanson, M.; Geoffroy, N. Natural Speciation of Ni, Zn, Ba and As in Ferromanganese Coatings on Quartz Using X-Ray Fluorescence, Absorption, and Diffraction. *Geochim. Cosmochim. Acta* **2007**, *71*, 95–128.

(17) Ronsbo, J. G. Coupled Substitutions Involving REEs and Na and Si in Apatites in Alkaline Rocks from the Ilimaussaq Intrusion, South Greenland, and the Petrological Implications. *Am. Miner.* **1989**, *74*, 896–901.

(18) Hughes, J. M.; Cameron, M.; Mariano, A. N. Rare-Earth-Element Ordering and Structural Variations in Natural Rare-Earth-Bearing Apatites. *Am. Miner.* **1991**, *76*, 1165–1173.

(19) Hughes, J. M.; Rakovan, J. F. Structurally Robust, Chemically Diverse: Apatite and Apatite Supergroup Minerals. *Elements* **2015**, *11*, 165–170.

(20) Fleet, M. E.; Pan, Y. M. Site Preference of Rare-Earth Elements in Fluorapatites. *Am. Miner.* **1995**, *80*, 329–335.

(21) Fleet, M.; Liu, X.; Pan, Y. Site Preference of Rare Earth Elements in Hydroxyapatite [$Ca_{10}(PO_4)_6(OH)_2$]. *J. Solid State Chem.* **2000**, *149*, 391–398.

(22) Gueriau, P.; Mocuta, C.; Bertrand, L. Cerium Anomaly at Microscale in Fossils. *Anal. Chem.* **2015**, *87*, 8827–8836.

(23) Glatzel, P.; Sikora, M.; Smolentsev, G.; Fernandez-Garcia, M. Hard X-Ray Photon-in Photon-out Spectroscopy. *Catal. Today* **2009**, *145*, 294–299.

(24) Kvashnina, K. O.; Butorin, S. M.; Glatzel, P. Direct Study of the F-Electron Configuration in Lanthanide Systems. *J. Anal. At. Spectrom.* **2011**, *26* (6), 1265–1272.

(25) Kotani, A.; Kvashnina, K.; Butorin, S.; Glatzel, P. A New Method of Directly Determining the Core-Hole Effect in the Ce L_3 XAS of Mixed Valence Ce Compounds-An Application of Resonant X-Ray Emission Spectroscopy. *J. Electron Spectrosc. Relat. Phenom.* **2011**, *184*, 210–215.

(26) Greinert, J. RV SONNE Fahrtbericht/Cruise Report SO242-1 JPI OCEANS Ecological Aspects of Deep-Sea Mining: DISCOL Revisited, Guayaquil - Guayaquil (Equador), 28.07.-25.08.2015. **2015**, 213 p. https://doi.org/10.3289/GEOMAR_REP_NS_26_2015.

(27) Haeckel, M.; Linke, P. RV SONNE Fahrtbericht/Cruise Report SO268 - Assessing the Impacts of Nodule Mining on the Deep-Sea Environment: NoduleMonitoring, Manzanillo (Mexico) – Vancouver (Canada), 17.02. – 27.05.2019. **2021**, 820 p. https://doi.org/10.3289/GEOMAR_REP_NS_59_20.

(28) Paul, S. A. L.; Haeckel, M.; Bau, M.; Bajracharya, R.; Koschinsky, A. Small-Scale Heterogeneity of Trace Metals Including Rare Earth Elements and Yttrium in Deep-Sea Sediments and Porewaters of the Peru Basin, Southeastern Equatorial Pacific. *Biogeosciences* **2019**, *16*, 4829–4849.

(29) Volz, J.; Mogollon, J.; Geibert, W.; Arbizu, P.; Koschinsky, A.; Kasten, S. Natural Spatial Variability of Depositional Conditions, Biogeochemical Processes and Element Fluxes in Sediments of the Eastern Clarion-Clipperton Check for Zone, Pacific Ocean. *Deep-Sea Res. I: Oceanogr. Res. Pap.* **2018**, *140*, 159–172.

(30) Haeckel, M.; Konig, I.; Reich, V.; Weber, M.; Suess, E. Pore Water Profiles and Numerical Modelling of Biogeochemical Processes in Peru Basin Deep-Sea Sediments. *Deep-Sea Res. II: Top. Stud. Oceanogr.* **2001**, *48*, 3713–3736.

(31) Paul, S. A. L.; Gaye, B.; Haeckel, M.; Kasten, S.; Koschinsky, A. Biogeochemical Regeneration of a Nodule Mining Disturbance Site: Trace Metals, DOC and Amino Acids in Deep-Sea Sediments and Pore Waters. *Front. Mar. Sci.* **2018**, *5*, n° 117.

(32) Mewes, K.; Mogollon, J.; Picard, A.; Ruhlemann, C.; Kuhn, T.; Nothen, K.; Kasten, S. Impact of Depositional and Biogeochemical Processes on Small Scale Variations in Nodule Abundance in the Clarion-Clipperton Fracture Zone. *Deep-Sea Res. I: Oceanogr. Res. Pap.* **2014**, *91*, 125–141.

(33) Bergmann, J. Rietveld Analysis Program BGMN. **2005**. http://www.bgmn.de/BGMN_manual_2005.pdf.

(34) Doebelin, N.; Kleeberg, R. Profex: A Graphical User Interface for the Rietveld Refinement Program BGMN. *J. Appl. Cryst.* **2015**, *48*, 1573–1580.

(35) Dulski, P. Interferences of Oxide, Hydroxide and Chloride Analyte Species in the Determination of Rare-Earth Elements in Geological Samples by Inductively-Coupled Plasma-Mass Spectrometry. *Fresenius J. Anal. Chem.* **1994**, *350*, 194–203.

(36) Garbe-Schonberg, D.; Muller, S. Nano-Particulate Pressed Powder Tablets for LA-ICP-MS. *J. Anal. Atom. Spectr.* **2014**, *29*, 990–1000.

(37) Jochum, K.; Garbe-Schonberg, D.; Veter, M.; Stoll, B.; Weis, U.; Weber, M.; Lugli, F.; Jentzen, A.; Schiebel, R.; Wassenburg, J.; Jacob, D.; Haug, G. Nano-Powdered Calcium Carbonate Reference Materials: Significant Progress for Microanalysis? *Geostand. Geoanalytical Res.* **2019**, *43* (4), 595–609.

(38) Gerin, C.; Gautheron, C.; Oliviero, E.; Bachelet, C.; Djimbi, D.; Seydoux-Guillaume, A.; Tassan-Got, L.; Sarda, P.; Roques, J.; Garrido, F. Influence of Vacancy Damage on He Diffusion in Apatite, Investigated at Atomic to Mineralogical Scales. *Geochim. Cosmochim. Acta* **2017**, *197*, 87–103.

(39) McLennan, S. M. Rare Earth Elements in Sedimentary Rocks: Influence of Provenance and Sedimentary Processes. *Rev. Miner.* **1989**, *21*, 169–200.

(40) Bau, M.; Schmidt, K.; Pack, A.; Bendel, V.; Kraemer, D. The European Shale: An Improved Data Set for Normalisation of Rare Earth Element and Yttrium Concentrations in Environmental and Biological Samples from Europe. *Appl. Geochem.* **2018**, *90*, 142–149.

(41) Goldoff, B.; Webster, J.; Harlov, D. Characterization of Fluor-Chlorapatites by Electron Probe Microanalysis with a Focus on Time-Dependent Intensity Variation of Halogens. *Am. Miner.* **2012**, *97*, 1103–1115.

(42) Batanova, V. G.; Sobolev, A. V.; Magnin, V. Trace Element Analysis by EPMA in Geosciences: Detection Limit, Precision and Accuracy. *IOP Conf. Ser. Mater. Sci. Eng.* **2018**, *304*, n° 012001.

(43) Manceau, A.; Simionovici, A.; Findling, N.; Glatzel, P.; Detlefs, B.; Wegorzewski, A. V.; Mizell, K.; Hein, J. R.; Koschinsky, A. Crystal Chemistry of Thallium in Marine Ferromanganese Deposits. *ACS Earth & Space Chem.* **2022**, *6*, 1269–1285.

(44) Proux, O.; Lahera, E.; Del Net, W.; Kieffer, I.; Rovezzi, M.; Testemale, D.; Irar, M.; Thomas, S.; Aguilar-Tapia, A.; Bazarkina, E.; Prat, A.; Tella, M.; Auffan, M.; Rose, J.; Hazemann, J. L. High-Energy Resolution Fluorescence Detected X-Ray Absorption Spectroscopy: A Powerful New Structural Tool in Environmental Biogeochemistry Sciences. *J. Environ. Qual.* **2017**, *46*, 1146–1157.

(45) Hazemann, J. L.; Proux, O.; Nassif, V.; Palancher, H.; Lahera, E.; Da Silva, C.; Braillard, A.; Testemale, D.; Diot, M. A.; Alliot, I.; Del Net, W.; Manceau, A.; Gelebart, F.; Morand, M.; Dermigny, Q.; Shukla, A. High-Resolution Spectroscopy on an X-Ray Absorption Beamline. *J. Synchr. Rad.* **2009**, *16*, 283–292.

(46) Paul, S. A. L.; Koschinsky, A. Solid Phase Trace Metal Geochemistry from Gravity Corer SO242/1_51-1 of SONNE Cruise SO242/1 at the DISCOL Area, Peru Basin. PANGAEA. **2019**, No. https://doi.org/10.1594/PANGAEA.902992, (accessed 20 December 2019).

(47) Iijima, K.; Yasukawa, K.; Fujinaga, K.; Nakamura, K.; Machida, S.; Takaya, Y.; Ohta, J.; Haraguchi, S.; Nishio, Y.; Usui, Y.; Nozaki, T.; Yamazaki, T.; Ichiyama, Y.; Ijiri, A.; Inagaki, F.; Machiyama, H.; Suzuki, K.; Kato, Y.; KR13-20 Cruise Members. Discovery of Extremely REY-Rich Mud in the Western North Pacific Ocean. *Geochem. J.* **2016**, *50*, 557–573.

(48) Bau, M.; Dulski, P. Distribution of Yttrium and Rare-Earth Elements in the Penge and Kuruman Iron-Formations, Transvaal Supergroup, South Africa. *Precambrian Res.* **1996**, *79*, 37–55.

(49) Bevington, P. R.; Robinson, D. K. *Data Reduction and Error Analysis for the Physical Sciences*; Mc Graw Hill: New York, NY, 2003.

(50) Bolhar, R.; Kamber, B.; Moorbath, S.; Fedo, C.; Whitehouse, M. Characterisation of Early Archaean Chemical Sediments by Trace Element Signatures. *Earth Planet Sc. Lett.* **2004**, *222*, 43–60.

(51) Bau, M.; Koschinsky, A.; Dulski, P.; Hein, J. R. Comparison of the Partitioning Behaviours of Yttrium, Rare Earth Elements, and Titanium between Hydrogenetic Marine Ferromanganese Crusts and Seawater. *Geochim. Cosmichim. Acta* **1996**, *60*, 1709–1725.

(52) Pan, Y.; Fleet, M. Compositions of the Apatite-Group Minerals: Substitution Mechanisms and Controlling Factors. In *Phosphates: Geochemical, Geobiological, and Materials Importance*; Kohn, M., Rakovan, J., Hughes, J., Eds.; 2002; Vol. 48, pp 13–49.

(53) Pasero, M.; Kampf, A.; Ferraris, C.; Pekov, I.; Rakovan, J.; White, T. Nomenclature of the Apatite Supergroup Minerals. *Eur. J. Miner.* **2010**, *22*, 163–179.

(54) Takahashi, Y.; Shimizu, H.; Usui, A.; Kagi, H.; Nomura, M. Direct Observation of Tetravalent Cerium in Ferromanganese Nodules and Crusts by X-Ray-Absorption near-Edge Structure (XANES). *Geochim. Cosmochim. Acta* **2000**, *64*, 2929–2935.

(55) Takahashi, Y.; Hayasaka, Y.; Morita, K.; Kashiwabara, T.; Nakada, R.; Marcus, M. A.; Kato, K.; Tanaka, K.; Shimizu, H. Transfer of Rare Earth Elements (REE) from Manganese Oxides to Phosphates during Early Diagenesis in Pelagic Sediments Inferred from REE Patterns, X-Ray Absorption Spectroscopy, and Chemical Leaching Method. *Geochem. J.* **2015**, *49*, 653–674.

(56) Janots, E.; Bernier, F.; Brunet, F.; Munoz, M.; Trcera, N.; Berger, A.; Lanson, M. Ce(III) and Ce(IV) (Re)Distribution and Fractionation in a Laterite Profile from Madagascar: Insights from in Situ XANES Spectroscopy at the Ce L-III-Edge. *Geochim. Cosmochim. Acta* **2015**, *153*, 134–148.

(57) Yu, C. X.; Drake, H.; Mathurin, F. A.; Astrom, M. E. Cerium Sequestration and Accumulation in Fractured Crystalline Bedrock: The Role of Mn-Fe (Hydr-)Oxides and Clay Minerals. *Geochim. Cosmochim. Acta* **2017**, *199*, 370–389.

(58) Hernandez-Viezcas, J.; Castillo-Michel, H.; Andrews, J.; Cotte, M.; Rico, C.; Peralta-Videa, J.; Ge, Y.; Priester, J.; Holden, P.; Gardea-Torresdey, J. In Situ Synchrotron X-Ray Fluorescence Mapping and Speciation of CeO_2 and ZnO Nanoparticles in Soil Cultivated Soybean (Glycine Max). *ACS Nano* **2013**, *7*, 1415–1423.

(59) Takahashi, Y.; Shimizu, H.; Kagi, H.; Yoshida, H.; Usui, A.; Nomura, M. A New Method for the Determination of Ce^{III}/Ce^{IV} Ratios in Geological Materials; Application for Weathering, Sedimentary and Diagenetic Processes. *Earth Planet. Sci. Lett.* **2000**, *182*, 201–207.

(60) Takahashi, Y.; Sakami, H.; Nomura, M. Determination of the Oxidation State of Cerium in Rocks by Ce L_{III}-Edge X-Ray Absorption near-Edge Structure Spectroscopy. *Anal. Chim. Acta* **2002**, *468*, 345–354.

(61) Takahashi, Y.; Sakashima, T.; Shimizu, H. Observation of Tetravalent Cerium in Zircon and Its Reduction by Radiation Effect. *Geophys. Res. Lett.* **2000**, *30*, n° 1137.

(62) Marcus, M.; Toner, B.; Takahashi, Y. Forms and Distribution of Ce in a Ferromanganese Nodule. *Marine Chem.* **2018**, *202*, 58–66.

(63) Manceau, A.; Merkulova, M.; Mathon, O.; Glatzel, P.; Murdzek, M.; Batanova, V.; Simionovici, A.; Steinmann, S. N.; Paktunc, D. The Mode of Incorporation of As(-I) and Se(-I) in Natural Pyrite Revisited. *ACS Earth Space Chem.* **2020**, *4*, 379–390.

(64) Filimonova, O. N.; Tagirov, B. R.; Trigub, A. L.; Nickolsky, M. S.; Rovezzi, M.; Belogub, E. V.; Reukov, V. L.; Vikentyev, I. V. The State of Au and As in Pyrite Studied by X-Ray Absorption Spectroscopy of Natural Minerals and Synthetic Phases. *Ore Geol. Rev.* **2020**, *121*.

(65) Konagaya, R.; Kawamura, N.; Yamaguchi, A.; Takahashi, Y. Highly-Sensitive Analysis of Fluorescence XANES at Europium (Eu) L_{III}-Edge for the Determination of Oxidation State for Trace Amount of Eu in Natural Samples by Bragg-Type Crystal Analyzer System. *Chem. Lett.* **2021**, *50*, 1570–1572.

(66) Merkulova, M.; Mathon, O.; Glatzel, P.; Batanova, V.; Marion, P.; Boiron, M. C.; Manceau, A. Revealing the Chemical Form of “Invisible” Gold in Natural Arsenian Pyrite and Arsenopyrite with High Energy-Resolution X-Ray Absorption Spectroscopy. *ACS Earth Space Chem.* **2019**, *3*, 1905–1914.

(67) Tagirov, B. R.; Trigub, A. L.; Kvashnina, K. O.; Shiryaev, A. A.; Chareev, D. A.; Nickolsky, M. S.; Abramova, V. D.; Kovalchuk, E. V. Covellite CuS as a Matrix for “Invisible” Gold: X-Ray Spectroscopic Study of the Chemical State of Cu and Au in Synthetic Minerals. *Geochim. Cosmochim. Acta* **2016**, *191*, 58–69.

(68) Trigub, A. L.; Tagirov, B. R.; Kvashnina, K. O.; Lafuerza, S.; Filimonova, O. N.; Nickolsky, M. S. Experimental Determination of Gold Speciation in Sulfide-Rich Hydrothermal Fluids under a Wide Range of Redox Conditions. *Chem. Geol.* **2017**, *471*, 52–64.

(69) Trigub, A. L.; Tagirov, B. R.; Kvashnina, K. O.; Chareev, D. A.; Nickckolsky, M. S.; Shiryaev, A. A.; Baranova, N. N.; Kovalchuk, E. V.; Mokhov, A. V. X-Ray Spectroscopy Study of the Chemical State of “Invisible” Au in Synthetic Minerals in the Fe-As-S System. *Am. Miner.* **2017**, *102*, 1057–1065.

(70) Pokrovski, G.; Escoda, C.; Blanchard, M.; Testemale, D.; Hazemann, J.; Gouy, S.; Kokh, M.; Boiron, M.; de Parseval, F.; Aigouy, T.; Menjot, L.; de Parseval, P.; Proux, O.; Rovezzi, M.; Beziat, D.; Salvi, S.; Kouzmanov, K.; Bartsch, T.; Pottgen, R.; Doert, T. An Arsenic-Driven Pump for Invisible Gold in Hydrothermal Systems. *Geochem. Pers. Lett.* **2021**, *17*, 39–44.

(71) Pokrovski, G.; Desmaele, E.; Laskar, C.; Bazarkina, E.; Testemale, D.; Hazemann, J.; Vuilleumier, R.; Seitsonen, A.; Ferlat, G.; Saitta, A. Gold Speciation in Hydrothermal Fluids Revealed by in Situ High Energy Resolution X-Ray Absorption Spectroscopy. *Am. Miner.* **2022**, *107*, 369–376.

(72) Le Pape, P.; Blanchard, M.; Juhin, A.; Rueff, J. P.; Ducher, M.; Morin, G.; Cabaret, D. Local Environment of Arsenic in Sulfide Minerals: Insights from High-Resolution X-Ray Spectroscopies, and First-Principles Calculations at the As K-Edge. *J. Anal. Atom. Spec.* **2018**, *33*, 2070–2082.

(73) Le Pape, P.; Stetten, L.; Hunault, M.; Mangeret, A.; Brest, J.; Boulliard, J. C.; Morin, G. HERFD-XANES Spectroscopy at the U M_4-Edge Applied to the Analysis of U Oxidation State in a Heavily Contaminated Wetland Soil. *Appl. Geochem.* **2020**, *122*, n° 104714.

(74) Seder-Colomina, M.; Mangeret, A.; Stetten, L.; Merrot, P.; Diez, O.; Julien, A.; Barker, E.; Thouveno, A.; Bargar, J.; Cazala, C.; Morin, G. Carbonate Facilitated Mobilization of

Uranium from Lacustrine Sediments under Anoxic Conditions. *Environ. Sci. Technol.* **2018**, *52*, 9615–9624.

(75) Manceau, A.; Merkulova, M.; Murdzek, M.; Batanova, V.; Baran, R.; Glatzel, P.; Saikia, B. K.; Paktunc, D.; Lefticariu, L. Chemical Forms of Mercury in Pyrite: Implications for Predicting Mercury Releases in Acid Mine Drainage Settings. *Environ. Sci. Technol.* **2018**, *52*, 10286–10296.

(76) Manceau, A.; Wang, J.; Rovezzi, M.; Glatzel, P.; Feng, X. Biogenesis of Mercury-Sulfur Nanoparticles in Plant Leaves from Atmospheric Gaseous Mercury. *Environ. Sci. Technol.* **2018**, *52*, 3935–3948.

(77) Madsen, I.; Scarlett, N.; Cranswick, L.; Lwin, T. Outcomes of the International Union of Crystallography Commission on Powder Diffraction Round Robin on Quantitative Phase Analysis: Samples 1a to 1h. *J. Appl. Cryst.* **2001**, *34*, 409–426.

(78) Leon-Reina, L.; Garcia-Mate, M.; Alvarez-Pinazo, G.; Santacruz, I.; Vallcorba, O.; de la Torre, A.; Aranda, M. Accuracy in Rietveld Quantitative Phase Analysis: A Comparative Study of Strictly Monochromatic Mo and Cu Radiations. *J. Appl. Cryst.* **2016**, *49*, 722–735.

(79) Liu, X.; Tournassat, C.; Grangeon, S.; Kalinichev, A. G.; Takahashi, Y.; Marques Fernadez, M. Molecular-Level Understanding of Metal Ion Retention in Clay-Rich Materials. *Nature Rev. Earth Environ.* **2022**, doi-org.insu.bib.cnrs.fr/10.1038/s43017-022-00301-z.

(80) Martin, J. M.; Nirel, P.; Thomas, A. J. Sequential Extraction Techniques - Promises and Problems. *Mar. Chem.* **1987**, *22*, 313–341.

(81) Nirel, P. M. V.; Morel, F. M. M. Pitfalls of Sequential Extractions. *Water Res.* **1990**, *24*, 1055–1056.

(82) Manceau, A.; Lanson, M.; Takahashi, Y. Mineralogy and Crystal Chemistry of Mn, Fe, Co, Ni, and Cu in a Deep-Sea Pacific Polymetallic Nodule. *Am. Miner.* **2014**, *99*, 2068–2083.

(83) Yamada, A.; Fons, P.; Matsubara, K.; Iwata, K.; Sakurai, K.; Niki, S. Electron Beam Probe Quantization of Compound Composition: Surface Phases and Surface Roughness. *Thin Solid Films* **2003**, *431*, 277–283.

(84) Newbury, D. Quantitative Electron Probe Microanalysis of Rough Targets: Testing the Peak-to-Local Background Method. *Scanning* **2004**, *26*, 103–114.

(85) Poirier, D.; Gauvin, R. X-Ray Microanalysis of Porous Materials Using Monte Carlo Simulations. *Scanning* **2011**, *33*, 126–134.

(86) Frank-Kamenetskaya, O.; Rozhdestvenskaya, I.; Rosseeva, E.; Zhuravlev, A. Refinement of Apatite Atomic Structure of Albid Tissue of Late Devon Conodont. *Crystallogr. Rep.* **2014**, *59*, 41–47.

(87) Yi, H.; Balan, E.; Gervais, C.; Segalen, L.; Fayon, F.; Roche, D.; Person, A.; Morin, G.; Guillaumet, M.; Blanchard, M.; Lazzeri, M.; Babonneau, F. A Carbonate-Fluoride Defect Model for Carbonate-Rich Fluorapatite. *Am. Miner.* **2013**, *98*, 1066–1069.

(88) Leventouri, T.; Chakoumakos, B.; Moghaddam, H.; Perdikatsis, V. Powder Neutron Diffraction Studies of a Carbonate Fluorapatite. *J. Mater. Res.* **2000**, *15*, 511–517.

(89) Schuffert, J.; Kastner, M.; Emanuelle, G.; Jahnke, R. Carbonate-Ion Substitution in Francolite: A New Equation. *Geochim. Cosmochim. Acta* **1990**, *54*, 2323–2328.

(90) Antonakos, A.; Liarokapis, E.; Leventouri, T. Micro-Raman and FTIR Studies of Synthetic and Natural Apatites. *Biomaterials* **2007**, *28*, 3043–3054.

(91) Marshall, A. O.; Marshall, C. P. Vibrational Spectroscopy of Fossils. *Paleotonlogy* **2015**, *58*, 201–211.

(92) Trotter, J. A.; Eggins, S. M. Chemical Systematics of Conodont Apatite Determined by Laser Ablation ICPMS. *Chem. Geol.* **2006**, *233*, 196–216.

(93) Camara, F.; Curetti, N.; Benna, P.; Abdu, Y. A.; Hawthorne, F. C.; Ferraris, C. The Effect of Type-B Carbonate Content on the Elasticity of Fluorapatite. *Phys. Chem. Miner.* **2018**, *45*, 789–800.

(94) Corona-Esquivel, R.; Levresse, G.; Sole, J.; Henriquez, F.; Pi, T. New Age in the Geological Evolution of the Cerro de Mercado Iron Oxide Apatite Deposit, Mexico: Implication in the Durango Apatite Standard (DAP) Age Variability. *J. S. Am. Earth Sci.* **2018**, *88*, 367–373.

(95) Ketcham, R. Technical Note: Calculation of Stoichiometry from EMP Data for Apatite and Other Phases with Mixing on Monovalent Anion Sites. *Am. Miner.* **2015**, *100* (7), 1620–1623.

(96) Knudsen, A.; Gunter, M. Sedimentary Phosphorites - An Example: Phosphoria Formation, Southeastern Idaho, USA. In *Phosphates: Geochemical, geobiological, and materials importance*; Kohn, M., Rakovan, J., Hughes, J., Eds.; 2002; Vol. 48, pp 363–389.

(97) Bertolus, M.; Defranceschi, M. Optimizing the Formula of Rare Earth-Bearing Materials: A Computational Chemistry Investigation. *Int. J. Quantum Chem.* **200AD**, *107*, 712–721.

FIGURE LEGENDS

Figure 1. Total REY concentration of seafloor sediment apatites measured in this study and by Takaya et al. (2018),[4] Liao et al. (2019, 2022),[3,5] and Bi et al. (2021),[2] using LA-ICP-MS.

Figure 2. REY_{SN} patterns. (a) Bulk sediments. (b) Clayey matrix and apatite grains of 51GC-695. (c) Apatite grains of the four sediments investigated in this study and of the sediment of the western North Pacific Ocean studied by Takaya et al. (2018).[4]

Figure 3. Ce L_3-edge XANES spectra. (a) Spectra of $Ce(III)NO_3 \cdot 6H_2O$ and a hydrogenetic crust (D20-1B[43]) as reference for Ce(IV)-MnO_2 measured at normal resolution with an energy-dispersive detector (EDD) and at high energy-resolution (HR-XANES) with a crystal-analyzer spectrometer (CAS).[44] (b) Hydrogenetic crust D20-1B and CeO_2 at normal and high resolution. (c) HR-XANES spectra of all apatite grains and the Durango apatite. (d) HR-XANES spectra of the bulk sediments.

Table 1. LA-ICP-MS REY concentrations (mg/kg) in the bulk sediments and apatites of the 16GC core from the CCZ and the 51GC core from the Peru Basin, and weight percentage of apatite in 51GC

	16GC-194				16GC-470				51GC-228				51GC-695							
	Bulk	Apatite			Bulk	Apatite			Bulk[b]	Apatite			Bulk[b]	Matrix			Apatite			Ratio Ap/Mat	%Ap
		Mean	SD[a]	RSD%		Mean	SD	RSD%		Mean	SD	RSD%		Mean	SD	RSD%	Mean	SD	RSD%		
La	47.6	3287	589	17.9	70.4	4009	675	16.8	38.4	1916	285	14.9	95.1	72.1	28.4	39.4	2530	534	21.1	35.1	0.9
Ce	71.0	2203	545	24.7	90.1	2081	414	19.9	42.8	1358	303	22.3	57.4	43.9	10.7	24.4	1005	287	28.6	22.9	1.4
Pr	14.0	966	184	19.1	20.6	1171	225	19.2	9.09	381	52.4	13.7	18.7	13.2	5.05	38.2	456	104	22.7	34.5	1.2
Nd	58.0	4723	904	19.1	85.2	5513	930	16.9	38.9	1913	276	14.4	83.5	63.0	24.8	39.4	2072	459	22.2	32.9	1.0
Sm	13.9	1287	240	18.7	20.6	1469	220	15.0	8.45	453	67.5	14.9	17.4	13.3	5.43	40.9	438	93.7	21.4	33.0	1.0
Eu	3.44	317	54.6	17.2	4.78	367	56.0	15.3	2.39	120	18.3	15.4	-	3.85	1.53	39.8	129	26.2	20.3	33.5	-
Gd	14.6	1548	254	16.4	21.9	1756	242	13.8	10.2	671	106	15.8	24.4	17.5	7.54	43.0	612	108	17.7	34.9	1.2
Tb	2.14	245	41.7	17.0	3.23	274	38.0	13.9	1.53	108	18.9	17.6	3.64	2.65	1.17	44.2	93.7	16.4	17.5	35.4	1.1
Dy	13.3	1590	267	16.8	19.6	1755	227	12.9	10.6	810	153	18.8	26.3	19.3	8.68	45.0	702	122	17.4	36.4	1.0
Y	69.4	8263	1235	15.0	107	9449	1329	14.1	75.1	6319	1100	17.4	216	158	78.4	49.7	6367	1030	16.2	40.4	0.9
Ho	2.52	276	46.9	17.0	3.78	308	40.1	13.0	2.35	164	30.8	18.8	6.25	4.01	1.87	46.6	167	28.4	17.0	41.7	1.4
Er	7.30	806	137	17.0	10.6	897	97.3	10.8	7.24	531	102	19.2	19.7	12.7	6.12	48.2	491	88.6	18.0	38.7	1.5
Tm	1.02	123	19.9	16.2	1.42	140	19.6	14.0	1.02	84.1	16.3	19.3	2.78	1.98	0.98	49.7	74.8	13.9	18.5	37.7	1.1
Yb	6.57	826	135	16.3	9.56	933	122	13.1	7.03	582	123	21.1	17.9	13.2	6.82	51.8	509	100	19.7	38.7	1.0
Lu	0.968	130	22.7	17.5	1.43	142	16.9	11.9	1.07	98.4	20.0	20.3	2.74	2.11	1.11	52.5	78.0	16.0	20.5	37.0	0.8
ΣREY	**326**	**26591**			**470**	**30265**			**256**	**15508**			**592**	**440**			**15726**		**Mean**	**35.5**	**1.1**
ΣREE	**256**	**18328**			**363**	**20816**			**181**	**9189**			**376**	**283**			**9358**		**SD**	**4.2**	**0.2**
Ratio[c]	**81.6**				**64.4**				**60.5**				**26.6**	**35.7**							
A1[d]	**0.63**	**0.29(8)[e]**			**0.55**	**0.22(5)**			**0.53**	**0.37(9)**			**0.31**	**0.33(12)**			**0.22(7)**				
A2[d]	**0.63**	**0.28(7)**			**0.54**	**0.22(5)**			**0.53**	**0.37(8)**			**0.31**	**0.33(9)**			**0.21(6)**				

[a]All standard deviations (SD) were calculated at 1 Std of the average, [b]51GC bulk sediment REY data are from Paul and Koschinsky (2019).[46] [c]Mean REY concentrations in apatites divided by the REY concentrations in the bulk sediment (16GC-194, 16GC-470,51GC-228) or the matrix (51GC-695),[d]Ce anomaly ,[e]The digits in parentheses are the standard deviation to the precision of the same number of least significant digits.

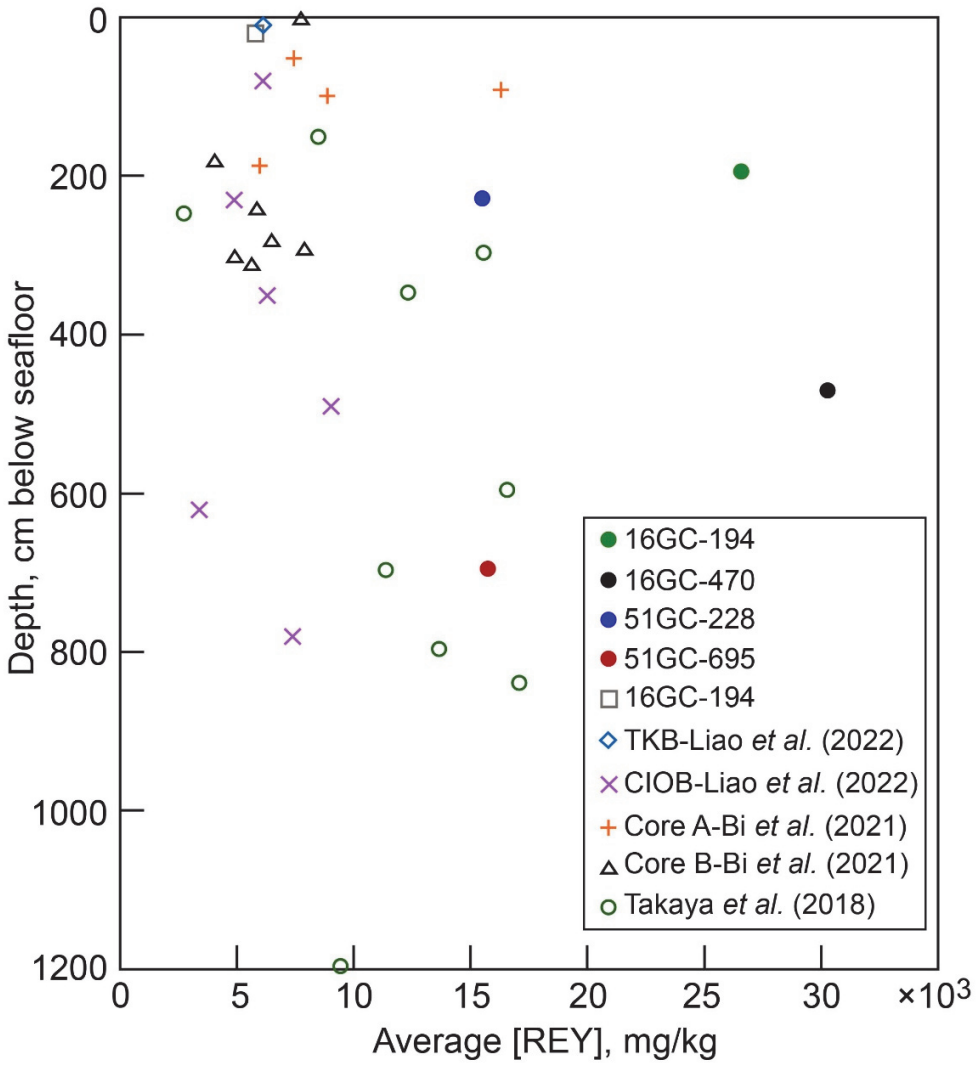
0
200
400
600
800
1000
1200
Depth, cm below seafloor
0
5
10
15
20
25
30
×10³
Average [REY], mg/kg
16GC-194
16GC-470
51GC-228
51GC-695
16GC-194
TKB-Liao et al. (2022)
CIOB-Liao et al. (2022)
Core A-Bi et al. (2021)
Core B-Bi et al. (2021)
Takaya et al. (2018)

Figure 1

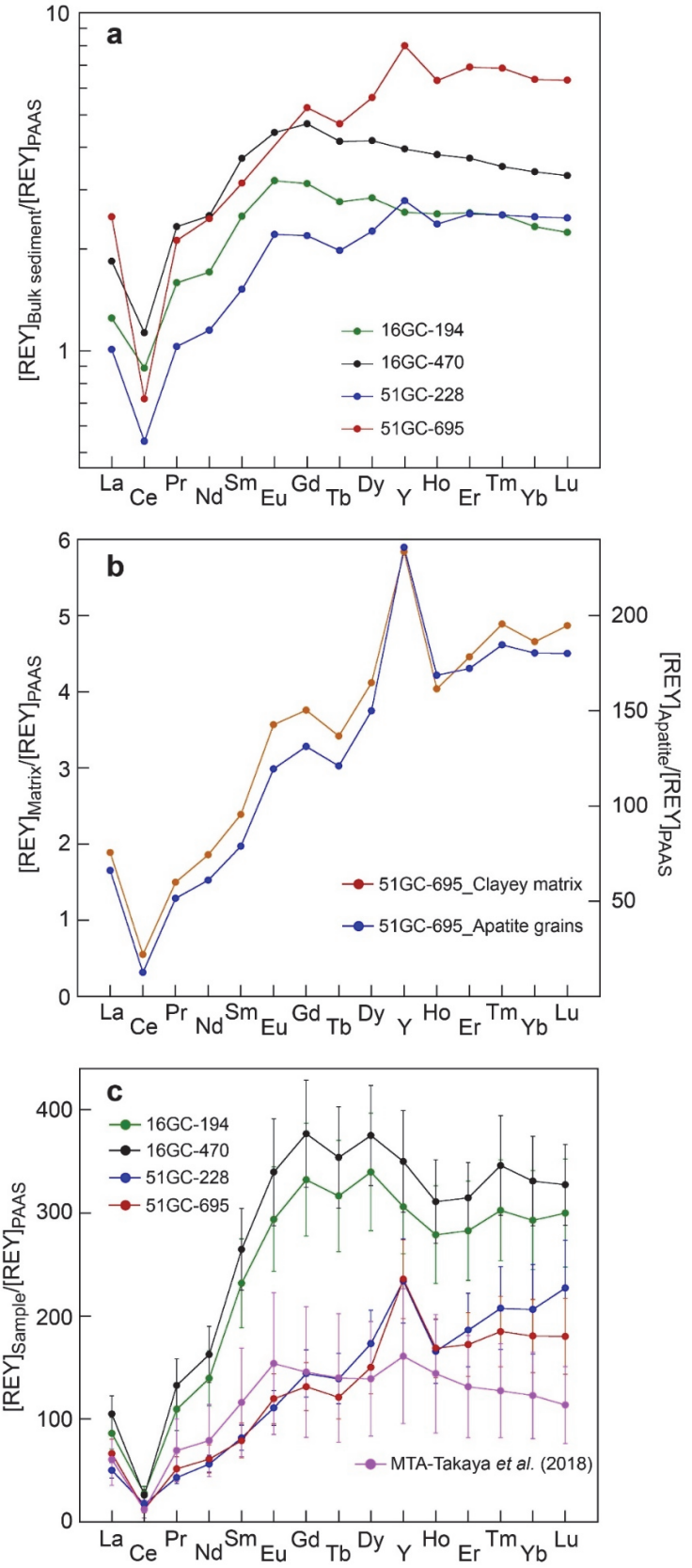
a
[REY]Bulk sediment/[REY]PAAS
16GC-194
16GC-470
51GC-228
51GC-695
La Ce Pr Nd Sm Eu Gd Tb Dy Y Ho Er Tm Yb Lu
b
[REY]Matrix/[REY]PAAS
[REY]Apatite/[REY]PAAS
51GC-695_Clayey matrix
51GC-695_Apatite grains
c
[REY]Sample/[REY]PAAS
MTA-Takaya et al. (2018)

Figure 2

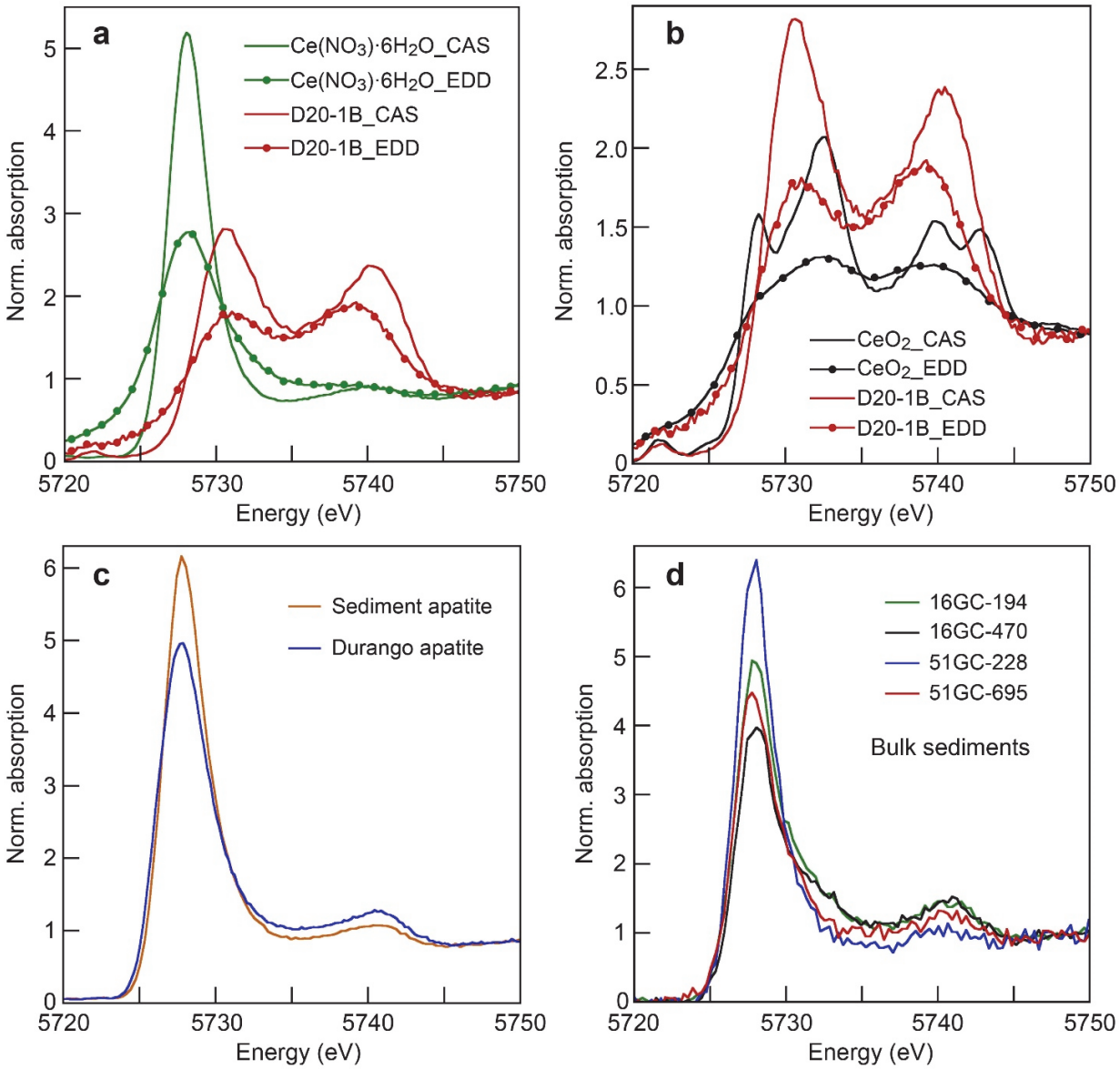
a
Ce(NO3)·6H2O_CAS
Ce(NO3)·6H2O_EDD
D20-1B_CAS
D20-1B_EDD
Norm. absorption
Energy (eV)
b
CeO2_CAS
CeO2_EDD
D20-1B_CAS
D20-1B_EDD
Norm. absorption
Energy (eV)
c
Sediment apatite
Durango apatite
Norm. absorption
Energy (eV)
d
16GC-194
16GC-470
51GC-228
51GC-695
Bulk sediments
Norm. absorption
Energy (eV)

Figure 3

Supporting Information

Fossil Bioapatites with Extremely High Concentrations of Rare Earth Elements and Yttrium from Deep-Sea Pelagic Sediments

Alain Manceau*[1], Sophie A.L. Paul[2,3], Alexandre Simionovici[1], Valérie Magnin[1], Mélanie Balvay[1], Nathaniel Findling[1], Mauro Rovezzi[4], Samuel Muller[5], Dieter Garbe-Schönberg[2,5], and Andrea Koschinsky[2]

[1]Université Grenoble Alpes, ISTerre, CNRS, CS40700, F-38058 Grenoble, France
[2]Department of Physics and Earth Sciences, Jacobs University Bremen, D-28759 Bremen, Germany
[3]GEOMAR, Helmholtz Centre for Ocean Research Kiel, Wischhofstr. 1-3, D-24148 Kiel, Germany
[4]Université Grenoble Alpes, CNRS, OSUG, FAME, F-38000 Grenoble, France
[5]CAU Kiel University, Institute of Geosciences, Ludewig-Meyn-Strasse 10, D-24118 Kiel, Germany

*Corresponding Author : alain.manceau@univ-grenoble-alpes.fr

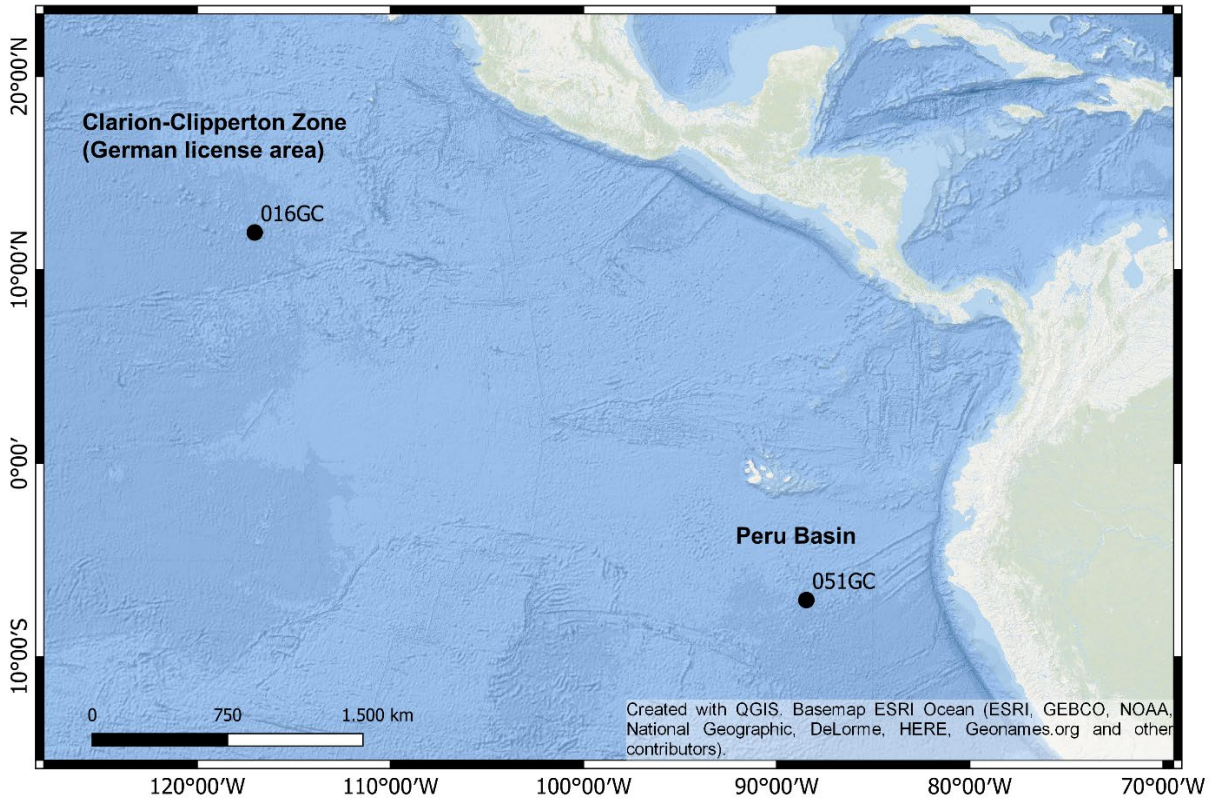

Figure S1. Geographical location of the two sediment cores.

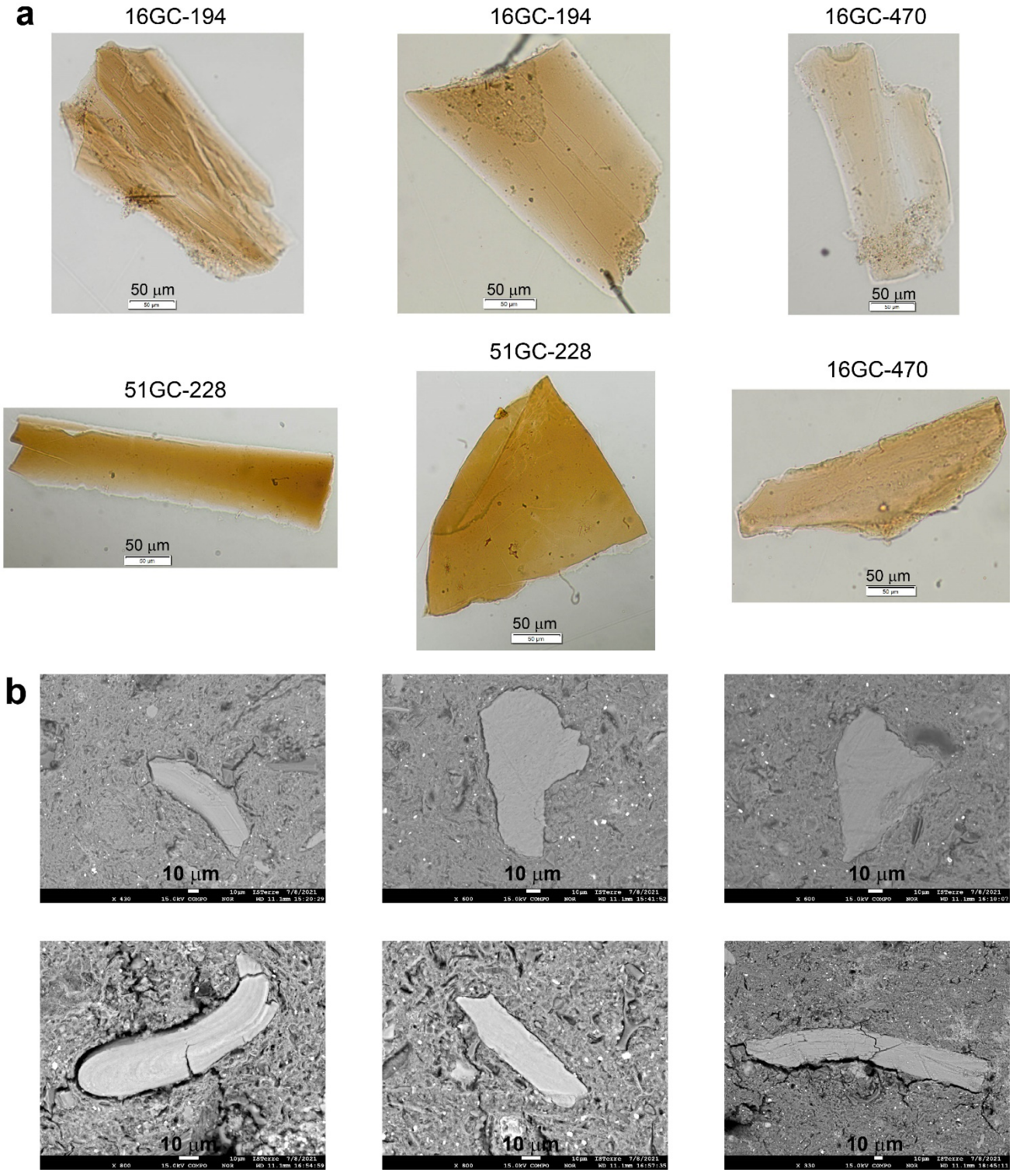

Figure S2. Optical (a) and backscattered electron (b) images of apatite grains in the seafloor sediments 16GC-194, 16GC-470, 51GC-228 (a), and 51GC-695 (b).

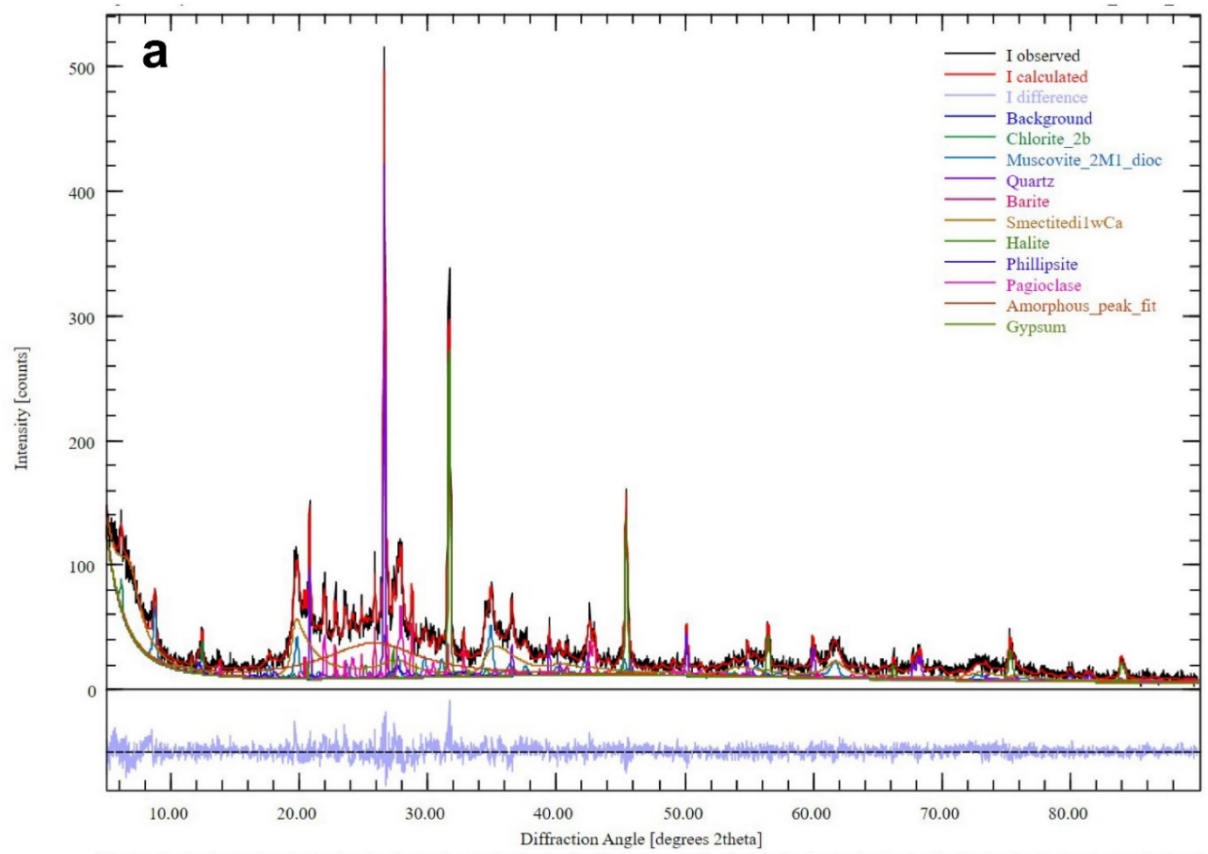
a
I observed
I calculated
I difference
Background
Chlorite_2b
Muscovite_2M1_dioc
Quartz
Barite
Smectitedi1wCa
Halite
Phillipsite
Pagioclase
Amorphous_peak_fit
Gypsum
Intensity [counts]
Diffraction Angle [degrees 2theta]

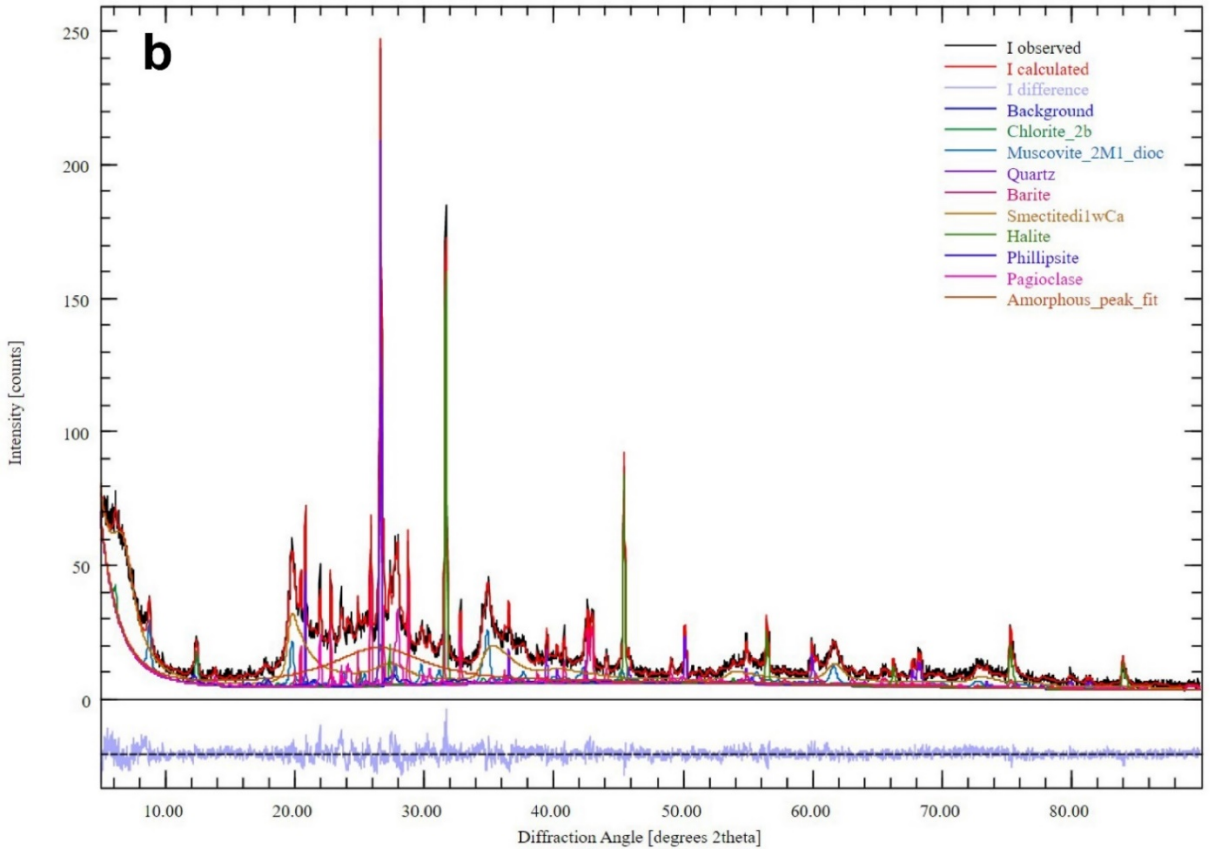
b
I observed
I calculated
I difference
Background
Chlorite_2b
Muscovite_2M1_dioc
Quartz
Barite
Smectitedi1wCa
Halite
Phillipsite
Pagioclase
Amorphous_peak_fit
Intensity [counts]
Diffraction Angle [degrees 2theta]

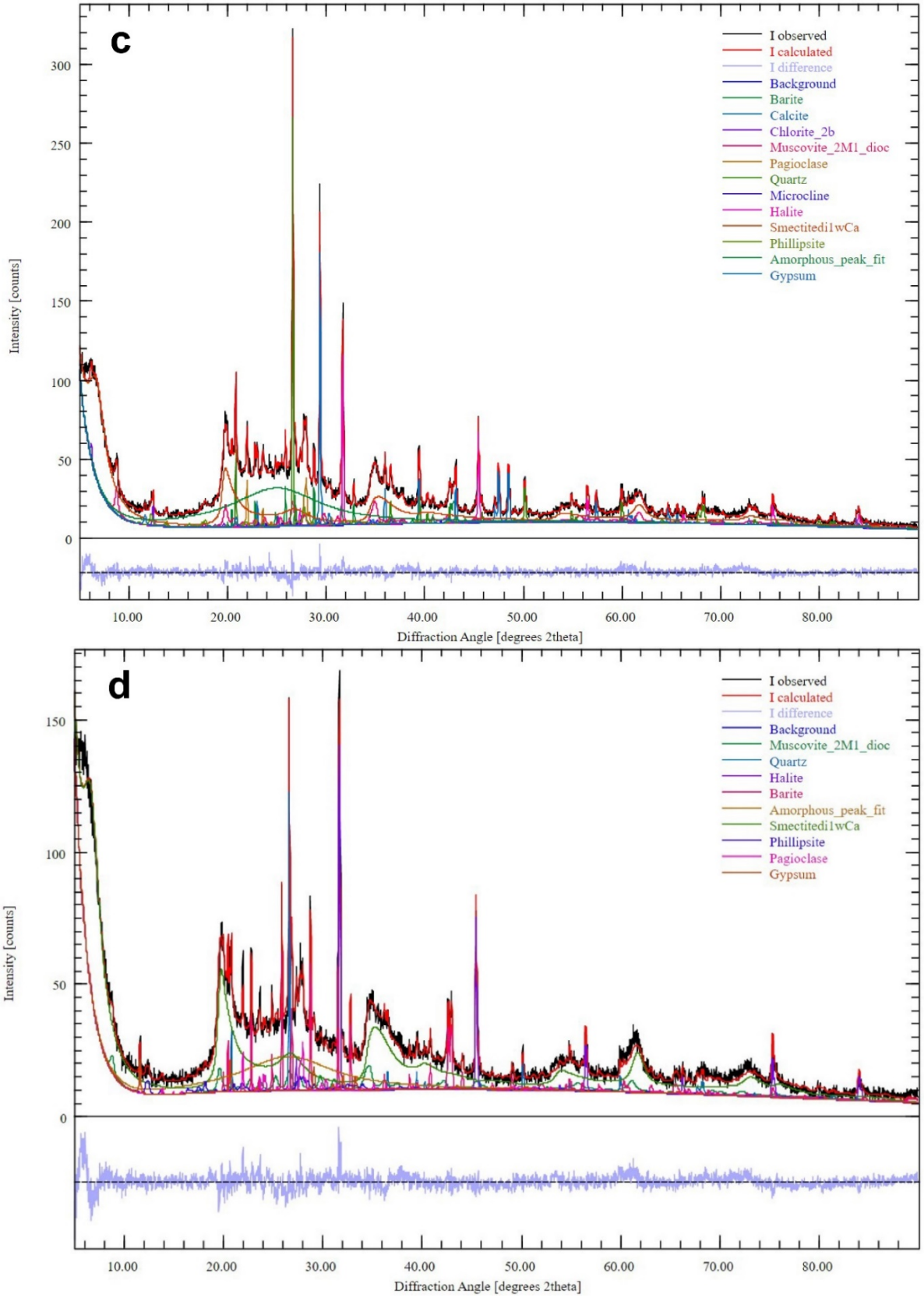

Figure S3. Rietveld-refined XRD patterns of 16GC-194 (a), 16GC-470 (b), 51GC-228 (c), and 51GC-695 (d). The purple-colored patterns at the bottom represent the residuals (difference between measured and calculated diffraction pattern). Step size: 0.026° 2θ, counting time = 12 s/pt.

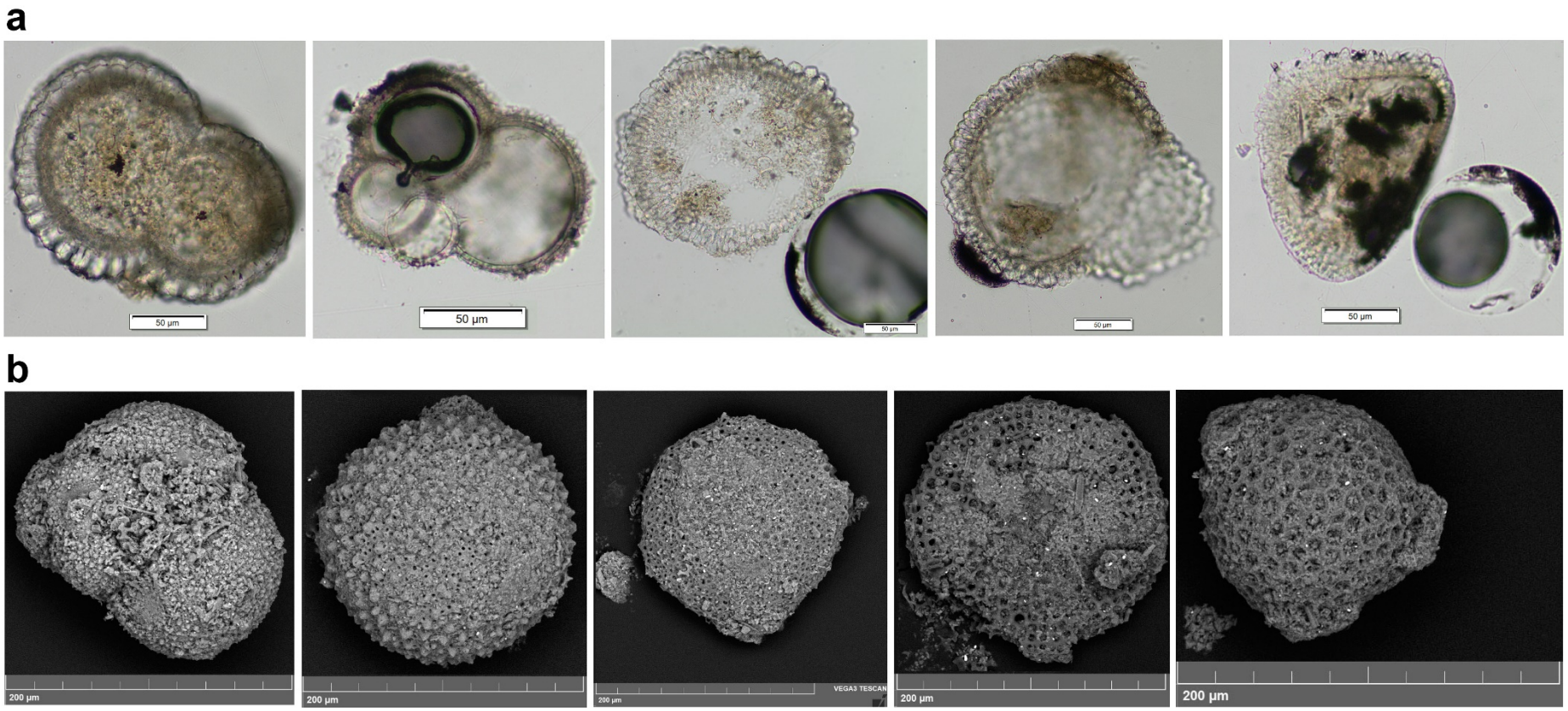

Figure S4: Optical (a) and backscattered electron (BSE, b) images of coccoliths from 51GC-228.

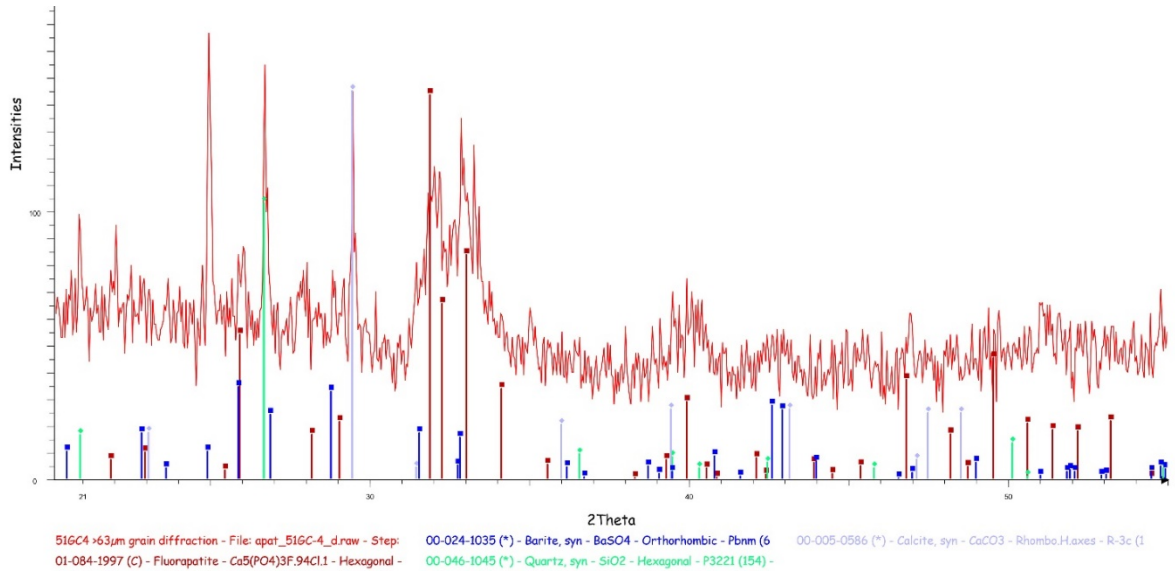

Figure S5. XRD pattern of the apatite grains of 51GC-228. Step size: 0.04° 2θ, counting time = 32 s/pt.

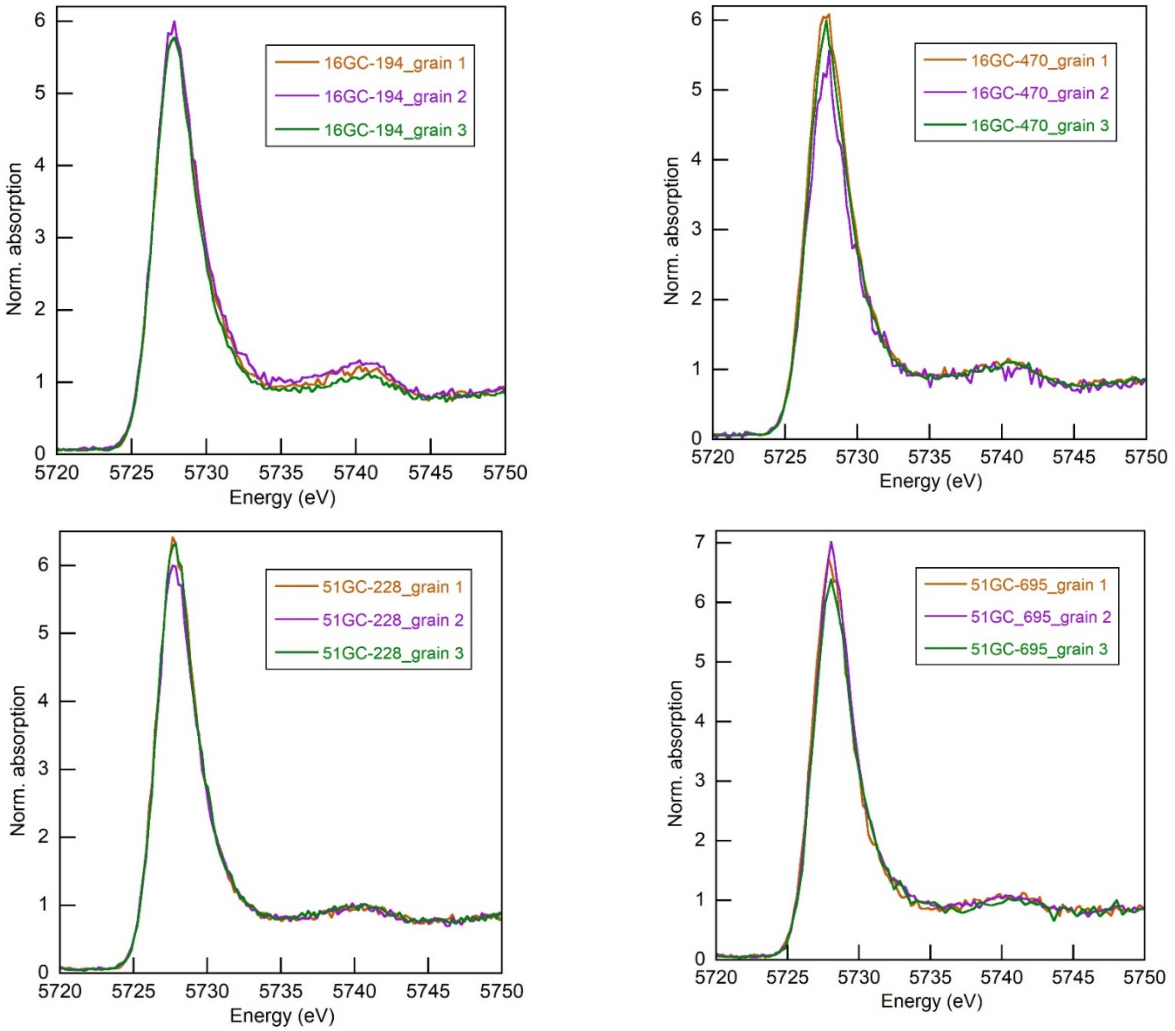

Figure S6. Ce L_3-edge HR-XANES spectra of individual apatite grains from the four sediments.

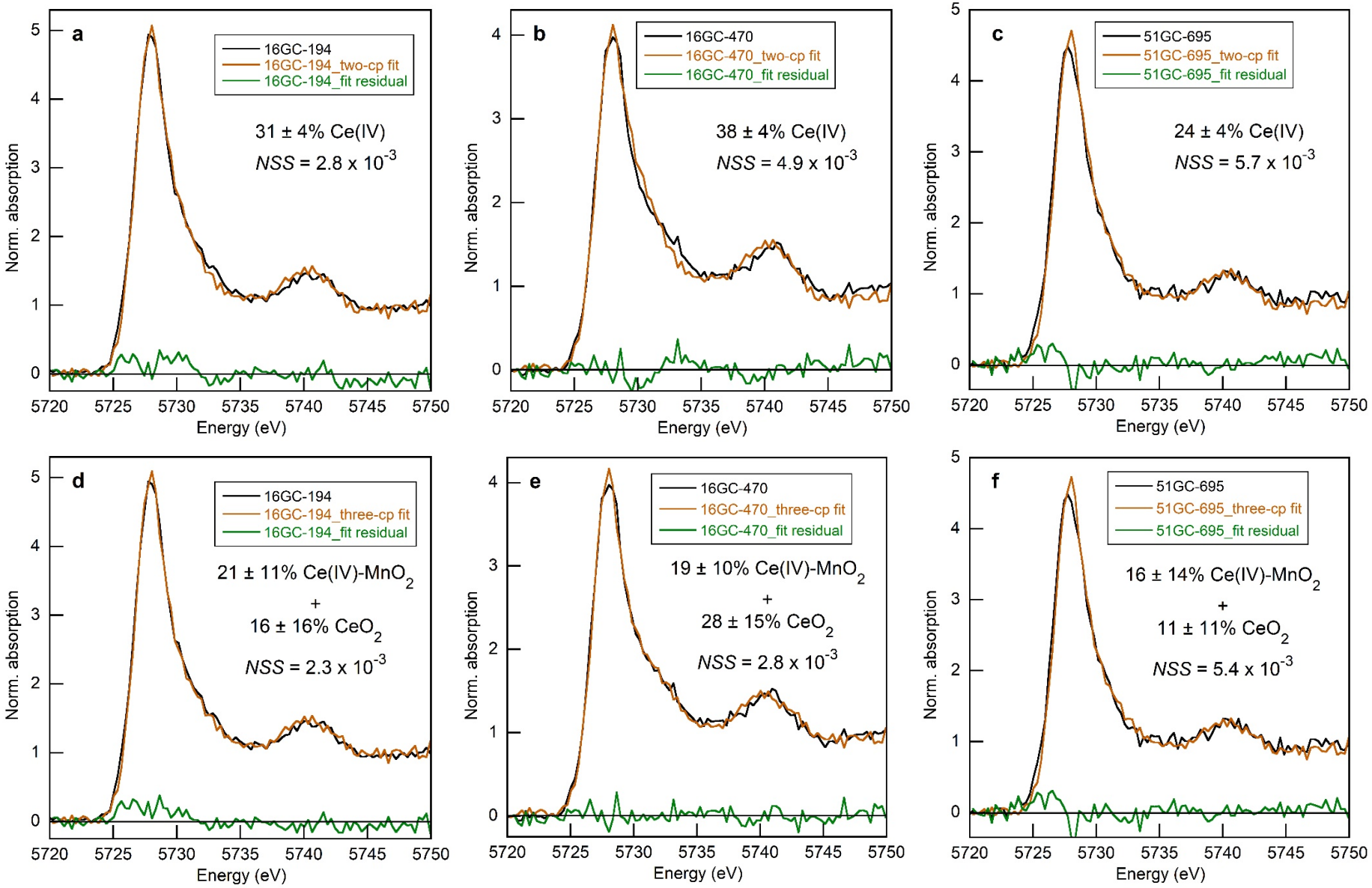
a
16GC-194
16GC-194_two-cp fit
16GC-194_fit residual
31 ± 4% Ce(IV)
NSS = 2.8 x 10-3
b
16GC-470
16GC-470_two-cp fit
16GC-470_fit residual
38 ± 4% Ce(IV)
NSS = 4.9 x 10-3
c
51GC-695
51GC-695_two-cp fit
51GC-695_fit residual
24 ± 4% Ce(IV)
NSS = 5.7 x 10-3
d
16GC-194
16GC-194_three-cp fit
16GC-194_fit residual
21 ± 11% Ce(IV)-MnO2
+
16 ± 16% CeO2
NSS = 2.3 x 10-3
e
16GC-470
16GC-470_three-cp fit
16GC-470_fit residual
19 ± 10% Ce(IV)-MnO2
+
28 ± 15% CeO2
NSS = 2.8 x 10-3
f
51GC-695
51GC-695_three-cp fit
51GC-695_fit residual
16 ± 14% Ce(IV)-MnO2
+
11 ± 11% CeO2
NSS = 5.4 x 10-3
Norm. absorption
Energy (eV)

Figure S7. Percentages of Ce(III) and Ce(IV) in the bulk sediments 16GC-194, 16GC-470, and 51C-695 determined by least-squares fits (LSF) of their Ce L_3-edge HR-XANES spectra. (a-c) Two-component fits with the spectra for the 51GC-228 bulk sediment (containing only Ce(III)) and for the D20-1B hydrogenetic nodule (Ce(IV)-MnO_2 reference). (d-f) Three-component fits with the 51GC-228 bulk sediment, the D20-1B, and the CeO_2 spectra. The precision of the percentages of Ce(III) and Ce(IV) in the fits was estimated to be equal to the variation of their best-fit values when the fit residual (*NSS*) was increased by 20%. *NSS* is the normalized sum-squared difference between the data and fit expressed as $\Sigma[(y_{data}-y_{fit})^2]/\Sigma(y_{data}^2)$. See detailed results in Table S4.

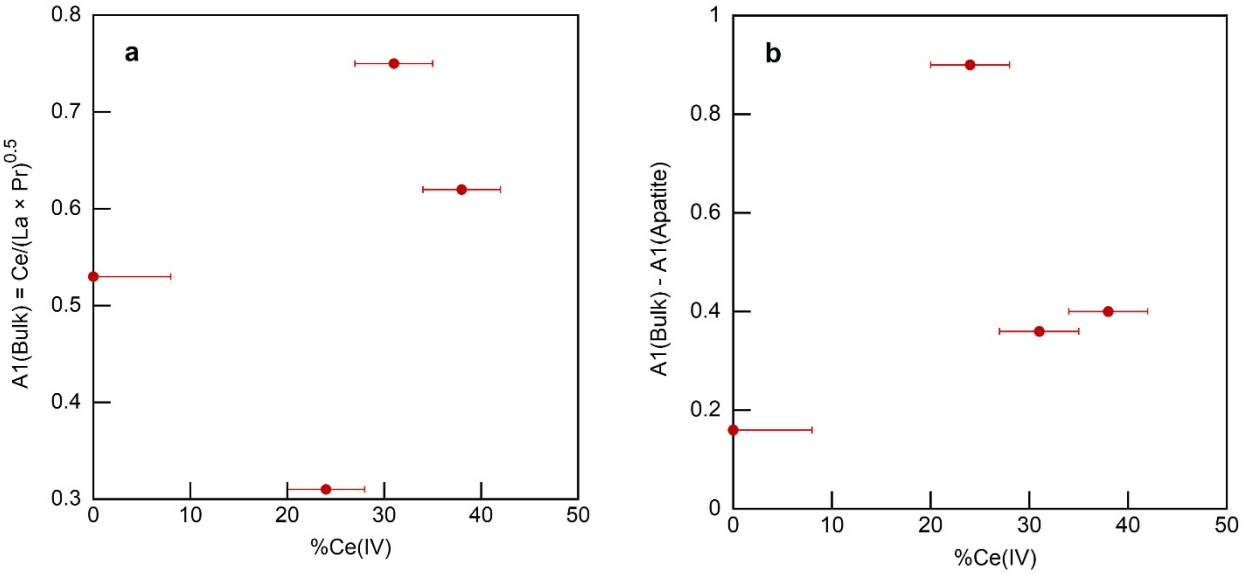

Figure S8. (a) Ce anomalies of the bulk sediments as a function of their percentage of Ce(IV) relative to total Ce. (b) Difference between the Ce anomalies of the bulk sediments and the constituent apatites as a function of the percentage of Ce(IV) relative to total Ce in the bulk sediments. The %Ce(IV) values are those from the 51GC-228 + D20-1B two-component fits in Table S4. Replacing the two-component fit %Ce(IV) value for 16GC-470 (38%) by the three-component fit value (47%, Table S4), does not change the interpretation of the data.

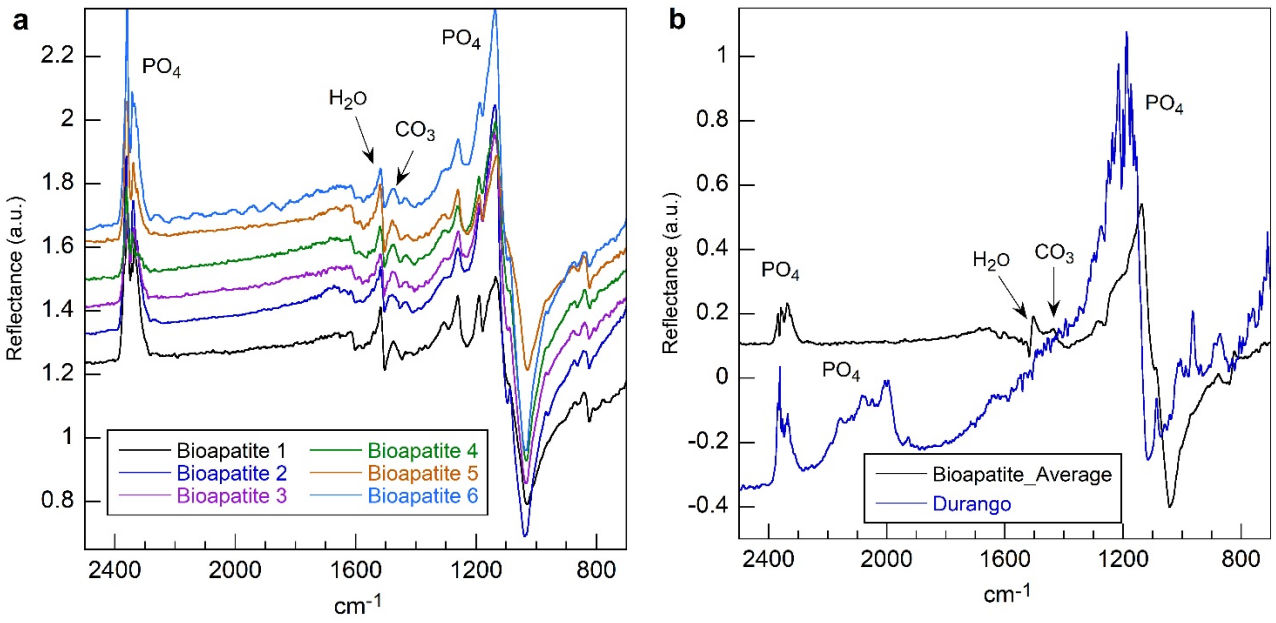

Figure S9. Infrared spectra measured in reflection mode of six bioapatites for 16GC-470 (a) and Durango apatite powder together with the average spectrum of the six bioapatites (b). A CO_3 peak is observed on the bioapatite spectra and not on the Durango apatite spectrum. The reflection peaks of PO_4 at 1000-1100 cm^{-1} and H_2O near 1500 cm^{-1} resemble a first derivative of a Gaussian peak, because the intensity of reflection is determined by the refractive index which has a minimum and a maximum on either side of the absorption bands (Yamamoto and Ishida, H. (1994) Optical theory applied to infrared spectroscopy. *Vibrational spectroscopy*, 8, 1-36).

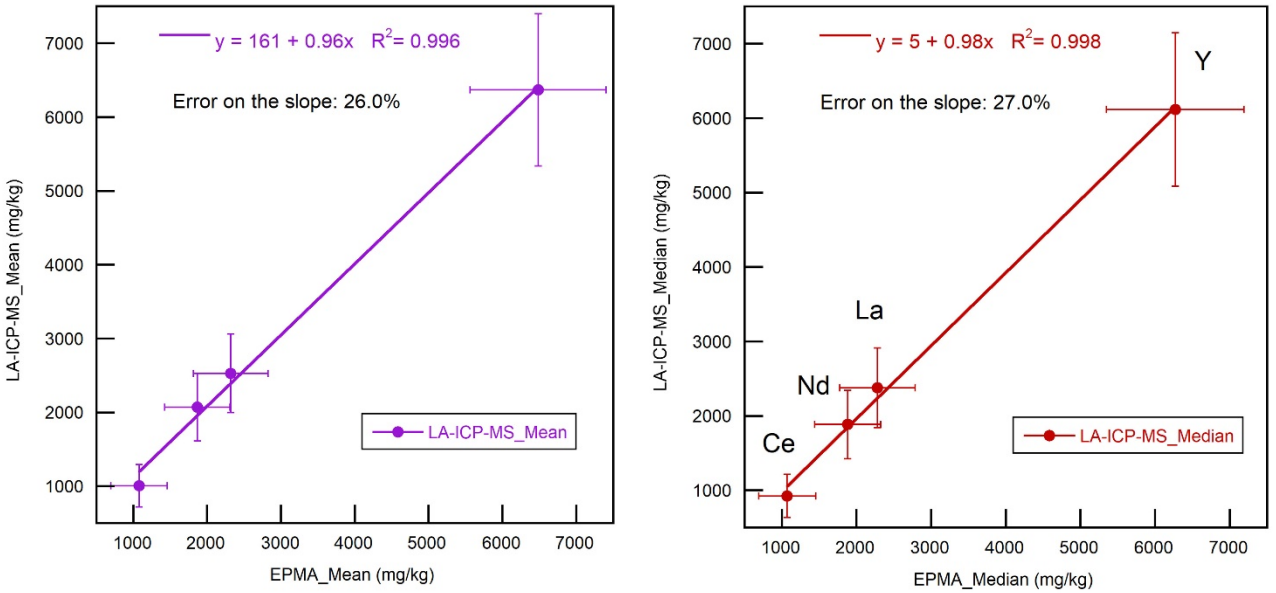

Figure S10. Concentrations of Ce, Nd, La, and Y in 12 apatite grains of sediment 51GC-695 measured by LA-ICP-MS and EPMA.